[redacted] (Memo)

Copy 3

NASA TM X-703

NASA TM X-703

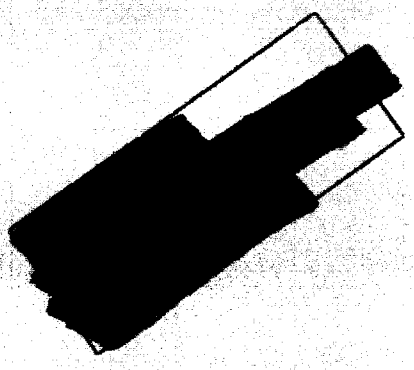

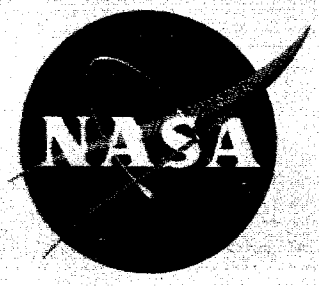

REMOVED FROM CATEGORY [redacted]
AUTHORITY- MEMO FROM
DROBKA TO LEBOW DATED [redacted]
JUN - 9 1966

TECHNICAL MEMORANDUM

X-703

HEAT-TRANSFER AND PRESSURE DISTRIBUTIONS ON A FLAT-FACE ROUNDED-CORNER BODY OF REVOLUTION WITH AND WITHOUT A FLAP AT A MACH NUMBER OF 8

By Robert A. Jones

Langley Research Center
Langley Station, Hampton, Va.

Declassified by authority of NASA
Classification Change Notices No. 67
Dated ** 6/29/66

DECLASSIFIED- AUTHORITY
U.S. 1286 DROBKA TO LEBOW
MEMO DATED
6/8/65

Microfiche (MF) _____

ff 653 July 65

GPO PRICE $ 2.50

CFSTI PRICE(S) $ .75

N66 33334

(ACCESSION NUMBER)	(THRU)
59	1
(PAGES)	(CODE)
TMX-703	33
(NASA CR OR TMX OR AD NUMBER)	(CATEGORY)

FACILITY FORM 602

[redacted]

NATIONAL AERONAUTICS AND SPACE ADMINISTRATION

WASHINGTON September 1962

[redacted]

NATIONAL AERONAUTICS AND SPACE ADMINISTRATION

TECHNICAL MEMORANDUM X-703

HEAT-TRANSFER AND PRESSURE DISTRIBUTIONS ON A FLAT-FACE ROUNDED-CORNER BODY OF REVOLUTION WITH AND WITHOUT A FLAP AT A MACH NUMBER OF 8*

By Robert A. Jones

SUMMARY

Heat-transfer and pressure distributions on a flat-face body of revolution with and without flap control were obtained at a Mach number of 8 and angles of attack from 0° to 45°. This body had a rounded corner, with a ratio of corner radius to body radius of 0.2, and an afterbody angle of 15°. The flap was located at the tangent line of the corner and afterbody. Reynolds numbers based on maximum body diameter were 0.22×10^6 and 0.93×10^6.

Results of the pressure tests indicated that the movement of the stagnation point with angle of attack was almost linear at low angles and that afterbody pressures for the windward ray were considerably higher than those predicted by modified Newtonian theory. Heat-transfer distributions on the body at 0° angle of attack were found to agree closely with predictions of a local similarity theory which used measured pressure distributions. Maximum measured heating rate, which always occurred at the corner, varied from 2.15 to 3.3 times the calculated heating rate of the stagnation point at 0° angle of attack as the angle of attack was varied from 0° to 45°. Heating rates to the flap varied widely and for several conditions the flap and the region of the body at the base of the flap had heating rates approximately equal to those at the stagnation point. The primary factor governing flap heating was found to be the angle between the flap surface and the free-stream flow direction.

*Title, Unclassified.

INTRODUCTION

Convective heating will have a dominant influence on the heat-shield design of the Apollo reentry vehicle. Predictions of the heat loads to be encountered are therefore necessary, but such predictions are presently hampered by a lack of experimental data. This report is concerned with the detailed distribution of heat transfer about a flat-face rounded-corner body of revolution and with the heat transfer to a flap-type control surface which could be used for maneuvering such a body. Tests were made at a Mach number of 8 with a maximum air enthalpy of 240 Btu/lb and Reynolds numbers based on maximum body diameter of 0.22×10^6 and 0.93×10^6.

The applicability of the data, obtained from an ideal gas, to high flight speeds where real-gas effects are encountered must therefore be considered. For a body without transition or separation, the test Mach number was sufficiently high to minimize the influence of Mach number on the results, and for equilibrium flow about the body the ideal-gas distribution is approximately equal to the real-gas distribution. However, the application of these test results to surfaces heated by boundary layers subject to transition, separation, reattachment, and so forth may not be justified since the effects of interplay of Reynolds number and enthalpy on such phenomena are not presently understood. Consequently, the data for the flap configurations may not be valid for high-speed reentry but may serve as a guide until high-enthalpy data become available.

SYMBOLS

C_p	pressure coefficient
$C_{p,max}$	maximum pressure coefficient
c	specific heat of model wall
c_p	specific heat of air at constant pressure
h	local heat-transfer coefficient
h_s	heat-transfer coefficient of stagnation point at 0° angle of attack
H_s	stagnation-point enthalpy

l	skin thickness
M_∞	free-stream Mach number
$N_{Pr,w}$	Prandtl number at wall
p	local static pressure
p_∞	free-stream static pressure
$p_{t,2}$	stagnation pressure behind normal shock
r_c	corner radius
r_b	body radius
R_∞	free-stream Reynolds number based on maximum body diameter
s	surface distance (see fig. 6)
T_w	wall temperature
T_r	recovery temperature
t	time
u	local velocity at edge of boundary layer
α	angle of attack
δ_F	flow deflection angle measured from free-stream flow direction
δ_f	flap deflection angle measured from back surface of flap to line parallel to model center line
θ	flap angle, measured from back surface of flap to free-stream flow direction
μ_w	air viscosity at wall conditions
μ_s	air viscosity at stagnation conditions
ρ_s	skin density
ρ_w	air density at wall conditions.

ρ_s air density at stagnation conditions

ϕ roll angle measured from windward plane of symmetry

ω angular location of stagnation point

TEST FACILITY

These tests were conducted in the Langley Mach 8 variable-density tunnel. This tunnel has an axisymmetric contoured nozzle terminating in an 18-inch-diameter test section. Stagnation pressures of approximately 165 and 915 lb/sq in. abs with corresponding stagnation temperatures of approximately 850° F and 950° F were used for the present tests. The resulting free-stream Reynolds numbers per inch were approximately 0.078×10^6 and 0.332×10^6, respectively. Under these conditions the Mach number in the tunnel test section was 7.95 ± 0.05 and 7.85 ± 0.05 at the high and low stagnation pressures.

The tunnel is adapted for transient testing by a model-injection mechanism which is located directly under the test section. (See fig. 1.) Models are strut-mounted to a plate which can be rapidly moved up or down by a pneumatic piston. The entire injection mechanism is enclosed in a sealed box; thus, the tunnel can continue running with the model in or out of the test section as well as while the model is being injected or retracted from the test section.

MODELS

The configurations tested consisted of a basic body and body-flap combinations. Photographs of the model are shown in figure 2, and sketches giving the pertinent dimensions and thermocouple and pressure orifice locations are presented in figures 3 and 4. The basic configuration was a flat-face body of revolution having a rounded corner and an afterbody angle of 15°. The ratio of the corner radius to the body radius was 0.2. The base of the flap was located at the tangent point of the afterbody and rounded corner.

Two sets of models made from 347 stainless steel were used; one contained pressure orifices, the other contained thermocouples. The pressure model had a thick wall with tubing soldered in holes and cut off flush with the outer surface so that the inside diameter of the tube (0.040 inch) formed the orifice. The thermocouple model had a nominal wall thickness of 0.030 inch; however, the actual thickness varied from

approximately 0.022 inch at the center of the face to 0.034 inch on the afterbody. To insure accurate data reduction, the wall thickness was measured within 0.001 inch at each s/r_b location. Thermocouples were made from No. 30 (American wire gage) iron-constantan wire and each wire of a thermocouple pair was soldered into a 0.013-inch-diameter hole. The holes of a thermocouple pair were spaced 0.020 inch between centers and located equidistant from the center of the face. The s/r_b locations were measured by placing wires in the holes and magnifying the profile 10 times by means of a profile-measuring projector before installation of the thermocouples. Figure 5 is a sketch of the corner profile magnified 10 times. A circle having a radius of 0.28 inch, the design radius of the corner, is shown for comparison with the actual profile. Although the maximum difference between the design radius and actual profile was only 0.005 inch, the actual tangent point of the front face and corner may have been displaced from the design tangent point as much as 0.040 inch. In terms of s/r_b this would be about 0.03.

DATA RECORDING

Thermocouple outputs were fed into a Beckman 210 high-speed analog to digital data recording system. This is a high-impedance system that samples the output voltage of each thermocouple at a rate of 40 times per second, converts it to a binary digital system, and records it on magnetic tape. For these tests the sensitivity of this system was 400 counts per millivolt which corresponds to 0.11° F per count. The background noise of the system was approximately ±3 counts; therefore, temperatures were recorded within $\pm 1/3^\circ$ F.

Pressures were measured by a mercury manometer. From photographs of the manometer the pressure was read within ±0.03 inch of mercury with a corresponding error in $p/p_{t,2}$ of about 0.2 percent. However, testing time was limited to about $1\frac{1}{2}$ minutes and the problem of error due to time required for the manometer to settle out was encountered for pressures lower than $p/p_{t,2} = 0.1$. The error in $p/p_{t,2}$ for pressures in this range may be as high as 1 percent.

Photographs of the flow about the model were taken by means of a single-path schlieren system using a light source having an effective flash duration of 4 microseconds. A horizontal wire was stretched across a window parallel to the tunnel center line as a reference to indicate the free-stream flow direction.

TEST TECHNIQUE AND DATA REDUCTION

Heat-transfer data were obtained by using a transient testing technique. The tunnel was started and brought to the desired operating conditions and then the model was rapidly injected into the airstream by a pneumatic piston. The time required for the model to travel through the tunnel boundary layer and for steady flow to be established was approximately 0.05 second. The model remained in the airstream only 2 or 3 seconds. Between tests it was cooled to room temperature by cold high-pressure air jets.

Heat-transfer coefficients were obtained by fitting a second-degree curve to the temperature-time data by the method of least squares and computing the time derivative of temperature on a card-programed computer. The local heat-transfer coefficient is given by the following equation:

$$h = \frac{\rho c l \frac{dt_w}{dt}}{T_r - T_w} \qquad (1)$$

where the temperature potential $T_r - T_w$ was taken to be the calculated recovery temperature minus the measured wall temperature. For the body data the recovery temperature was calculated by assuming a laminar recovery factor of 0.85 and isentropic expansion of the flow from the stagnation point to the measured local wall pressure. A recovery factor of 1 was assumed for the flap data. A complete description of the curve-fitting procedure and data-reduction method is given in reference 1.

For the present tests heat-transfer coefficients were computed for the time interval from 0.1 to 0.5 second after injection of the model into the airstream. At these short times the temperature of the model surface was within a few degrees of its temperature prior to injection. The maximum variation in surface temperature was usually much less than 20° F at the time for which data were reduced. This nearly isothermal surface together with the thin skin of the model helped to keep heat-conduction effects to a minimum. Inasmuch as heat conduction was thought to be negligible, no heat-conduction corrections have been applied to the data of these tests. The accuracy of the heat-transfer coefficients computed by equation (1) was affected by the accuracy of the values used for ρ, c, and l as well as by the data recording mentioned previously. It is thought that the heat-transfer coefficients are accurate within 15 percent; however, any errors in ρ and c would be constants and therefore affect only the level and not the distribution.

RESULTS AND DISCUSSION

The general orientation of the model with the free stream and the nomenclature used throughout the report are shown in figure 6. The angle of attack was taken to be that angle between the center line of the model and the free-stream flow direction. When the flap was in the location shown in figure 6, it was called the leeward flap; when the flap was 180° from this position, it was called the windward flap. For both locations the flap hinge line was at the tangent line of the rounded corner and afterbody.

Flow Field

Schlieren photographs of the flow are shown in figures 7, 8, and 9. As can be seen in these photographs the sting was almost as wide as the base of the model; however, it was slender in cross section and sharpened on both edges (fig. 2) so as to disturb the flow as little as possible. The sting had no appreciable effect on the body shock wave; however, at angles of attack a small shock wave was formed on the windward side where apparently the separated flow from the rear of the afterbody reattached to the sting (fig. 7). This phenomenon was thought to have no effect on the data presented herein.

The schlieren photographs of the flow about the body-flap configuration (fig. 8) indicate that for the leeward flap the flow separated from the body at the corner and reattached to the flap with a shock wave forming near the point of reattachment. The location on the flap where this shock wave appears to originate did not move much with a change in angle of attack; however, the angle between this shock wave and the surface of the flap became less as the angle of attack was increased. When the flap was located on the windward side of the model (fig. 9), the flow pattern was entirely different. For this location the tip of the flap was sometimes the most forward part of the body-flap combination. At 45° angle of attack and a flap deflection angle δ_f of 90° the shock wave was attached to the tip of the flap and the flow direction was inward toward the body; however, the body corner caused the flow to separate at about the midchord of the flap.

Pressure Distributions

The pressure data of the body configuration are presented in figure 10. The movement of the stagnation point with angle of attack as determined from these data is shown in figure 11. Note that the stagnation point does not jump suddenly to the corner at an angle of attack,

as Newtonian theory would predict, but moves gradually and almost linearly at low angles. An angle of attack of almost 45° was reached before the stagnation point had moved to the Newtonian stagnation point.

The variation of afterbody pressure with angle of attack is shown in figure 12. At $\phi = 0^\circ$ the data were considerably higher than those obtained by use of modified Newtonian theory which predicts the pressure

$$\frac{p}{p_{t,2}} = \sin^2\delta_F + \frac{p_\infty}{p_{t,2}} \cos^2\delta_F \qquad (2)$$

For values of ϕ larger than 90° the pressure was almost invariant with angle of attack and was greater than free-stream pressure; however, at these low pressures, the error due to the time required for the manometer to settle out may have been significant.

Pressure distributions on the body-flap configurations are presented in figures 13 and 14. The vertical dashed line at $s/r_b = 1.06$ denotes the location of the base of the flap and the solid symbols indicate the pressure distribution on the body only configuration of figure 10. Pressure data were taken along the center line of the flap only. There were several conditions for which the pressure on the flap was higher than the total pressure behind a normal shock wave $\left(p/p_{t,2} > 1\right)$. This phenomenon indicates that the low total-pressure flow, which had passed through the normal portion of the shock wave, had been washed away from the flap by cross flow. Thus, the flow over the flap passed through an oblique portion of the shock wave and had lower entropy (higher total pressure). The effect of the flap on the pressure distribution over the body was generally confined to that portion of the rounded corner between s/r_b of 0.8 and the base of the flap. In this region there was usually an increase in pressure. One exception to this increase in pressure on the body at the base of the flap was the data of figure 14(c). This exception was probably due to the attached oblique shock (fig. 9) and flow direction discussed previously. The primary factor in determining the pressure on the flap appeared to be the angle between the flap surface and the free-stream flow direction θ. The variation of pressure on the center of the flap as a function of θ is presented in figure 15. Also shown in this figure is the modified Newtonian pressure variation $C_p/C_{p,max} = \sin^2\theta$.

Heat-Transfer Distribution

Heat-transfer distributions on the basic body are shown in figure 16 as the ratio h/h_s (h is the measured local heat-transfer coefficient

and h_s is the calculated heat-transfer coefficient for the stagnation point at 0° angle of attack). The stagnation-point heat-transfer coefficient h_s was computed by the local similarity theory of reference 2 as

$$h_s = \frac{c_p}{778}(0.768)\left(N_{Pr,w}\right)^{-0.6}\left(\rho_w\mu_w\right)^{0.10}\left(\rho_s\mu_s\right)^{0.40}\left(\frac{du}{ds}\right)_{s=0}^{1/2} \qquad (3)$$

where $(du/ds)_{s=0}$ was determined from the relation $u/\sqrt{2H_s} = 0.168s/r_b$ found experimentally in reference 3 for a flat-face body at a free-stream Mach number of 4.95 (assumed invariant with Mach number for $M_\infty \geq 5$). This relation was used rather than the measured pressure data because no special care was taken to determine the stagnation-point velocity gradient in these tests. The theory curve shown in figure 16(a) was obtained by using a velocity gradient determined from the pressure data of figure 8 and the method of reference 2. Local velocities were computed at each station by using perfect gas relations and were plotted as a function of s/r_b. The velocity gradient was the slope of the curve faired through these data. This procedure resulted in a velocity gradient at the stagnation point about 8 percent higher than that given by the relation of reference 3.

The distribution of heat transfer predicted by the theory for 0° angle of attack agrees well with the measured data; however, the level predicted by the theory is about 17 percent low at the stagnation point. Part of this difference (about 4 percent) in level is accounted for by the difference between the stagnation-point velocity gradient of reference 3 (used in reducing the data) and the velocity gradient computed from pressure data (used in the theoretical pressure distribution).

The change in experimental heat-transfer distribution with Reynolds number was small and the data of both Reynolds numbers are believed to be for conditions of laminar flow. The low Reynolds number data at an angle of attack of 45° were omitted from figure 16(d) since schlieren photographs showed that the model created separation of the tunnel boundary layer and that the shock wave from this separation impinged on the model. Maximum heating always occurred in the $\phi = 0$ plane (windward plane of symmetry) between $s/r_b = 0.8$ and 0.9. The heat-transfer-coefficient ratio h/h_s in this area was 2.15 at 0° angle of attack and increased steadily to a maximum of 3.3 at 45° angle of attack.

Variation of afterbody heating with angle of attack is shown in figure 17 for $s/r_b = 1.3$. Since data were not obtained at a value of s/r_b of 1.3 for all values of ϕ, this figure was prepared by fairing

a curve through the data of figure 16 and plotting the faired values. The heating to the windward ray ($\phi = 0^\circ$) varied from $h/h_s = 0.06$ at 0° angle of attack to $h/h_s = 0.9$ at 45° angle of attack. At $\phi = 90^\circ$ the heat-transfer rate increased only slightly with angle of attack. For values of ϕ larger than 90° the heat-transfer rate was low $\left(h/h_s < 0.1\right)$ and appeared to decrease slightly with angle of attack until a minimum was reached at $\alpha = 30^\circ$; it then increased with further increases in angle of attack.

The flow field in the region of the flap was complex; separation and reattachment were usually present. This complicated flow pattern was expected to have a dominating influence on the heat transfer to the flap and to the body in the region near the flap. A qualitative indication of the heating to this area was obtained by coating wood models with a temperature-sensitive paint and taking high-speed motion pictures of the color patterns formed when the model was suddenly injected into and heated by the hot airstream. An example of the results of this technique is shown in figure 18. The photographs in figure 18(a) were made by enlarging three frames of the 16-millimeter high-speed color film exposed during the test. The paint used actually changed color three times (pink to blue to yellow and finally to olive green). An indication of the color changes, and therefore the relative heating rates, can be seen as different shades from light gray to black. For clarity, these color changes are shown by an artist's sketch in figure 18(b). An angle of attack of 45° and flap deflection angle of 120° were used for illustration inasmuch as these conditions caused some of the highest heating rates on the leeward flap and on the body at the base of the flap. The stagnation point was at the forward corner of the body which is shown at the bottom of the photographs and illustrated in the following sketch:

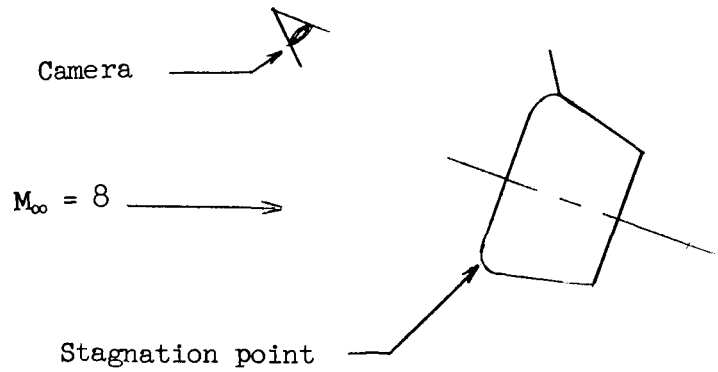

The effects of separation and reattachment on the heat-transfer distribution on the flap were evident. A clearly defined region of high

heating is evident on the flap where the flow reattached and this high-heating area extended outward to the tip of the flap. A small area having a high heating rate also existed on the body corner at the base of the flap. The heating rate to these areas was approximately equal to the stagnation-point heating rate (nearly simultaneous color change).

Heat-transfer distributions on the flap-body configurations are presented in figures 19 and 20. The data for the body only, shown as solid symbols, were taken from figure 16 and are shown here so that the effect of the flap on the heating to the body can be determined. The location of the base of the flap is noted in the figures by the dashed lines at $s/r_b = 1.06$. In general, the variation of heat transfer across the span of the flap was small; however, for the leeward flap there was a trend of higher heating at the edges for a value of s/r_b of 1.47 particularly at low angles of attack (fig. 19(a)). The variation of heat transfer along the chord of the flap was found to be rather large for some conditions; for example, the leeward flap at an angle of attack of 45° and flap deflection angle of 120° (fig. 19(d)). These conditions were the same as those for the temperature-sensitive-paint patterns shown in figure 18. The heating rate to the base of the flap was approximately one-half the heating rate to the remainder of the flap. This phenomenon was believed to be due to reattachment of the separated flow somewhere between a value of s/r_b of 1.2 and 1.34.

The effects of the flap on the heat transfer to the body were confined to a region between s/r_b of 0.8 and the base of the flap. The heating in this region was increased by the presence of the flap, the increase depending on the flap deflection angle, and was, for several conditions, the highest heating found on the body-flap configuration especially for the windward-flap configuration.

The primary factor in the flap heat-transfer rate appeared to be the angle between the flap surface and the free-stream flow direction θ. The variation of the average heating rate to the center portion of the flap as a function of θ is presented in figure 21. A strong dependence of heat transfer to the leeward flap on flap angle θ was evident. This dependency was similar to that of the flap pressure shown in figure 15. Heat transfer to the windward and leeward flaps appeared to be of the same order; however, the range of flap angles was not the same.

CONCLUSIONS

Heat-transfer and pressure distributions on a flat-face body of revolution with and without flap control were obtained at a Mach number

of 8 and angles of attack from 0° to 45°. This body had a rounded corner, with a ratio of corner radius to body radius of 0.2, and an afterbody angle of 15°. Results of the investigation indicated that the following conclusions can be made:

1. The stagnation point did not jump suddenly to the corner at an angle of attack, as Newtonian theory would predict, but moved gradually and almost linearly at low angles of attack. The afterbody pressure along the windward ray at angles of attack was considerably higher than that predicted by modified Newtonian theory.

2. The heat-transfer distribution at 0° angle of attack was in close agreement with that predicted by a local similarity theory using measured pressure distributions. Maximum heating always occurred in the vicinity of the corner. As the angle of attack varied from 0° to 45° the maximum measured heating rate varied from 2.15 to 3.3 times the calculated heating rate of the stagnation point at 0° angle of attack. The afterbody heating rate of the windward ray reached a value at 45° angle of attack that was 0.9 that of the stagnation point at 0° angle of attack.

3. Heat-transfer rates to a flap located at the tangent point of the corner and afterbody were found, under certain conditions, to be approximately equal to the stagnation-point value. The flow pattern about the body-flap configuration was found to be complex; separation and reattachment were usually present. Although the flap heat transfer was very sensitive to the location of the separation and reattachment points, the primary factor appeared to be the angle between the flap surface and the free-stream flow direction. The flap was found to cause an increase in the heat transfer to the body in the region near the base of the flap. For several conditions this was the region of highest heating found on the body-flap configuration.

Langley Research Center,
National Aeronautics and Space Administration,
Langley Station, Hampton, Va., May 28, 1962.

REFERENCES

1. Jones, Robert A., and Gallagher, James J.: Heat-Transfer and Pressure Distributions of a 60° Swept Delta Wing With Dihedral at a Mach Number of 6 and Angles of Attack From 0° to 52°. NASA TM X-544, 1961.

2. Beckwith, Ivan E., and Cohen, Nathaniel B.: Application of Similar Solutions to Calculations of Laminar Heat Transfer on Bodies With Yaw and Large Pressure Gradient in High-Speed Flow. NASA TN D-625, 1961.

3. Cooper, Morton, and Mayo, Edward E.: Measurements of Local Heat Transfer and Pressure on Six 2-Inch-Diameter Blunt Bodies at a Mach Number of 4.95 and at Reynolds Numbers Per Foot up to 81×10^6. NASA MEMO 1-3-59L, 1959.

[redacted]

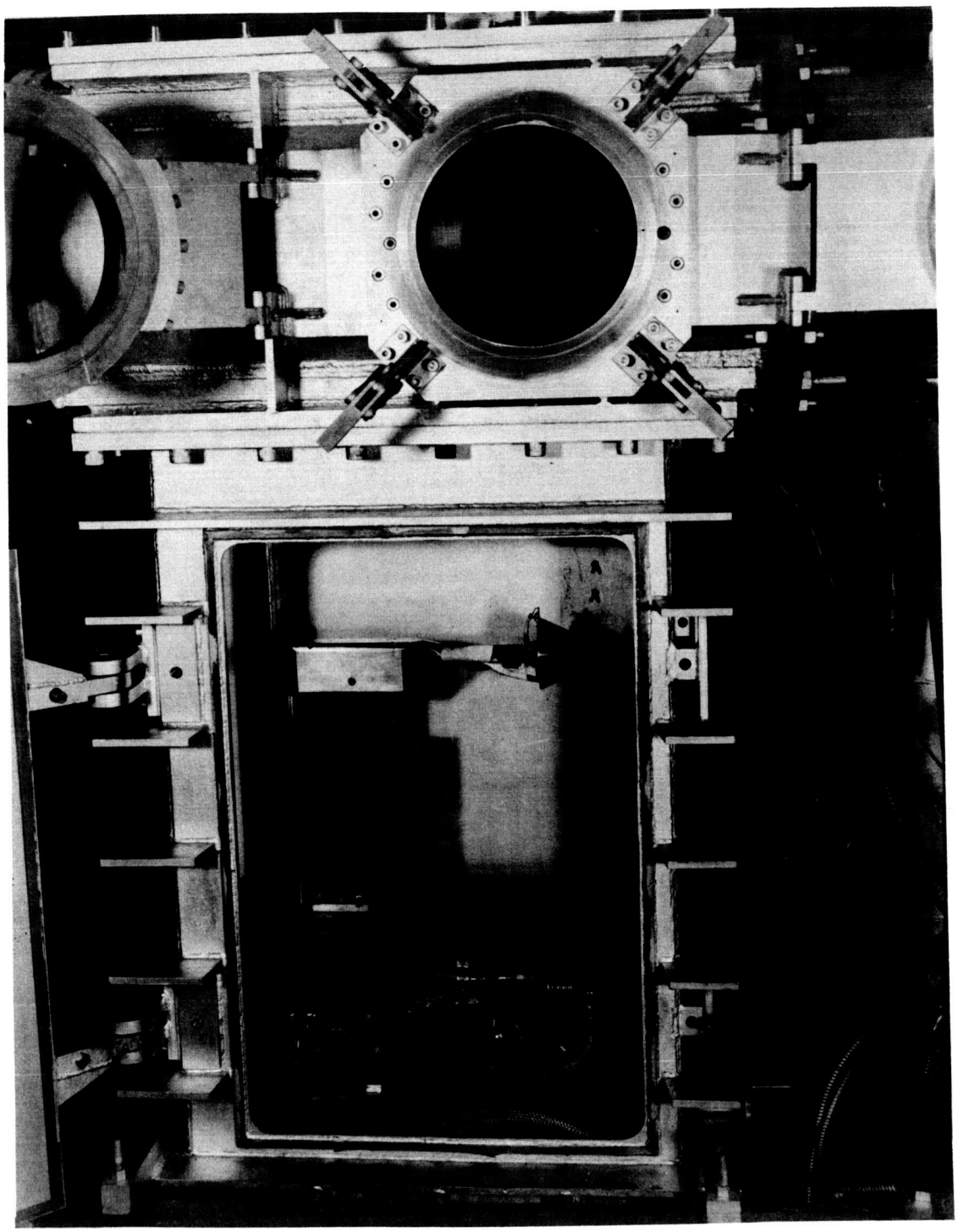

Figure 1.- Test section and injection mechanism. L-61-2863

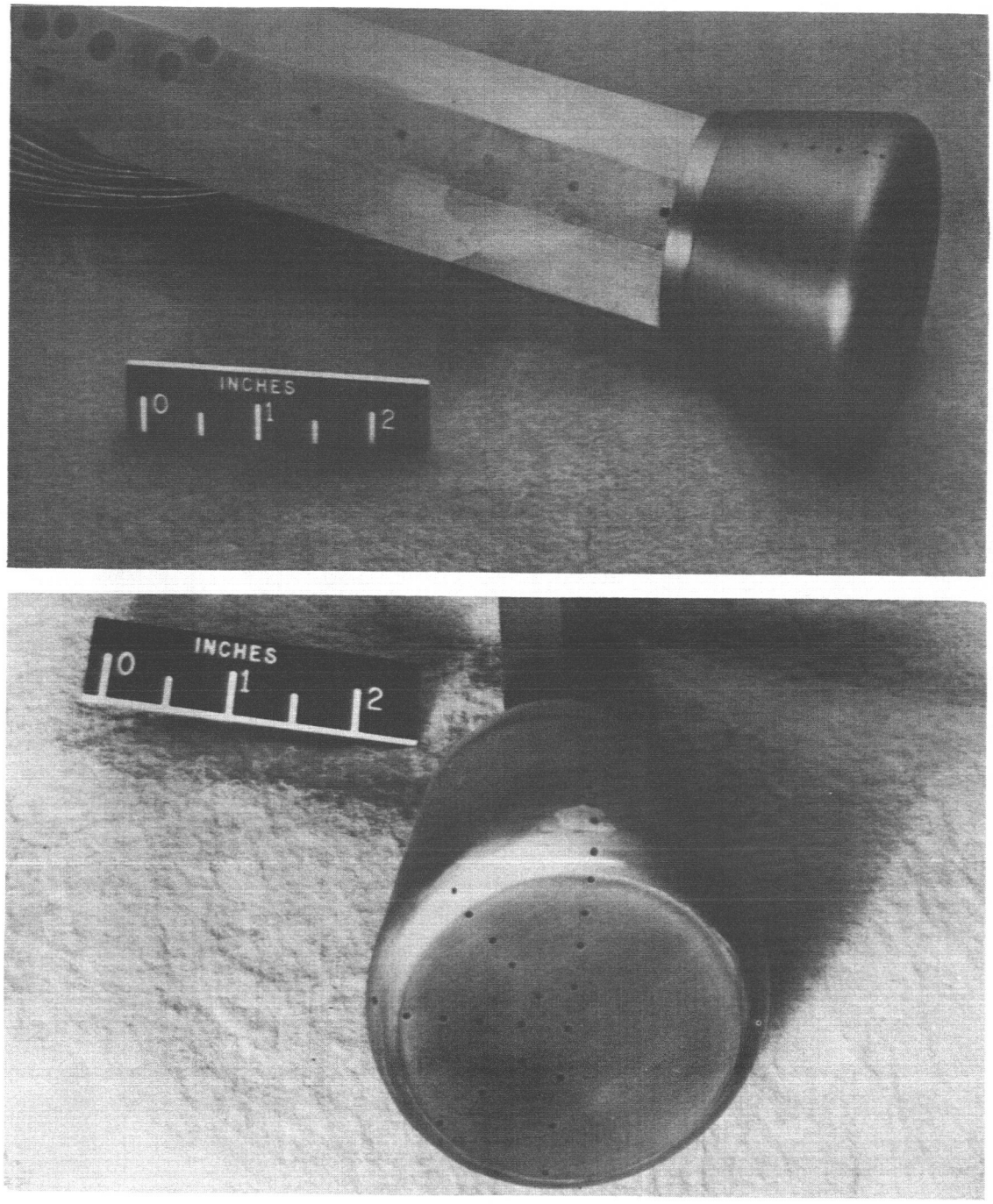

Figure 2.- Model used in the investigation. L-62-2079

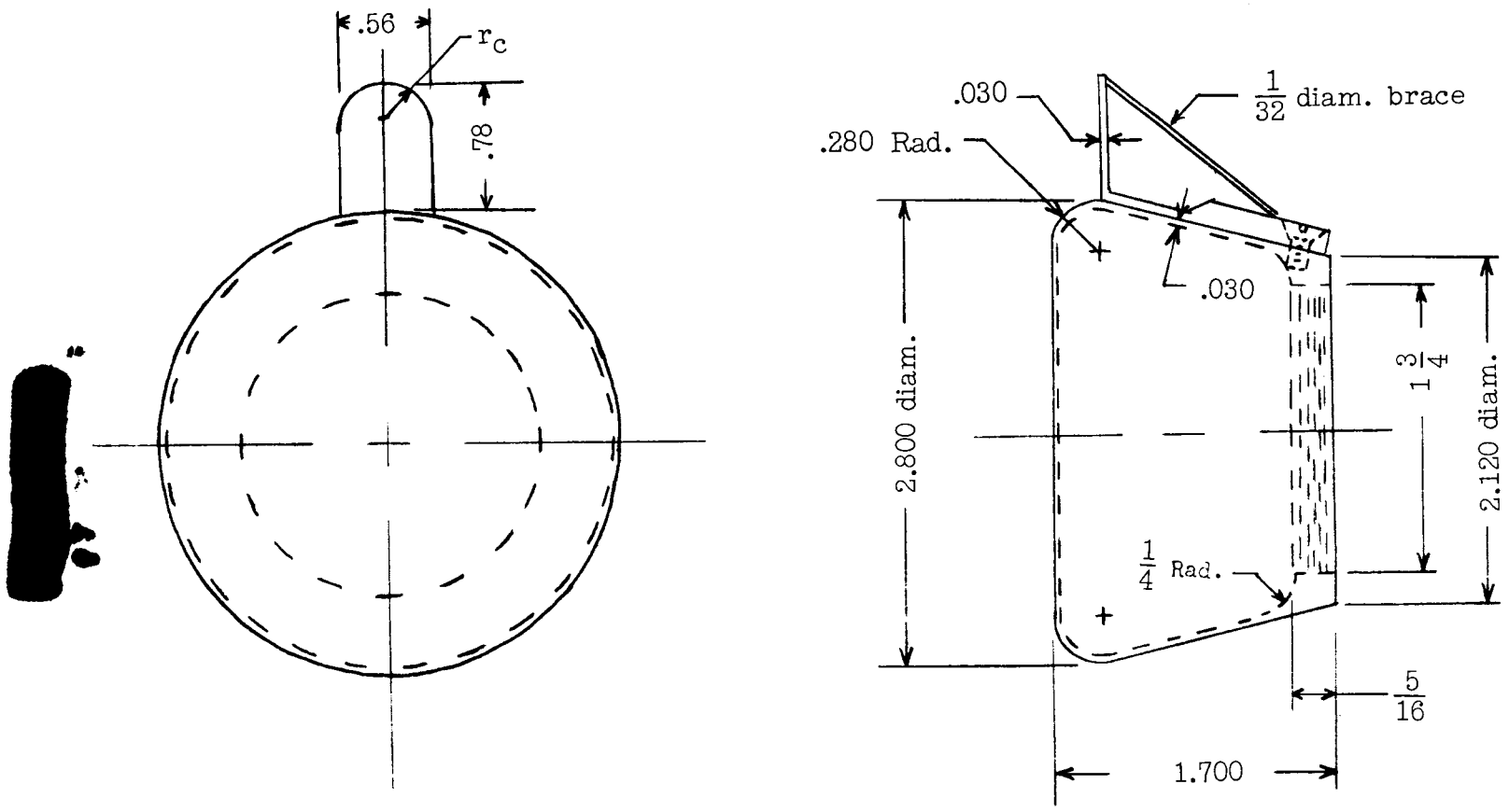

Figure 3.- Sketch of model. All dimensions are in inches.

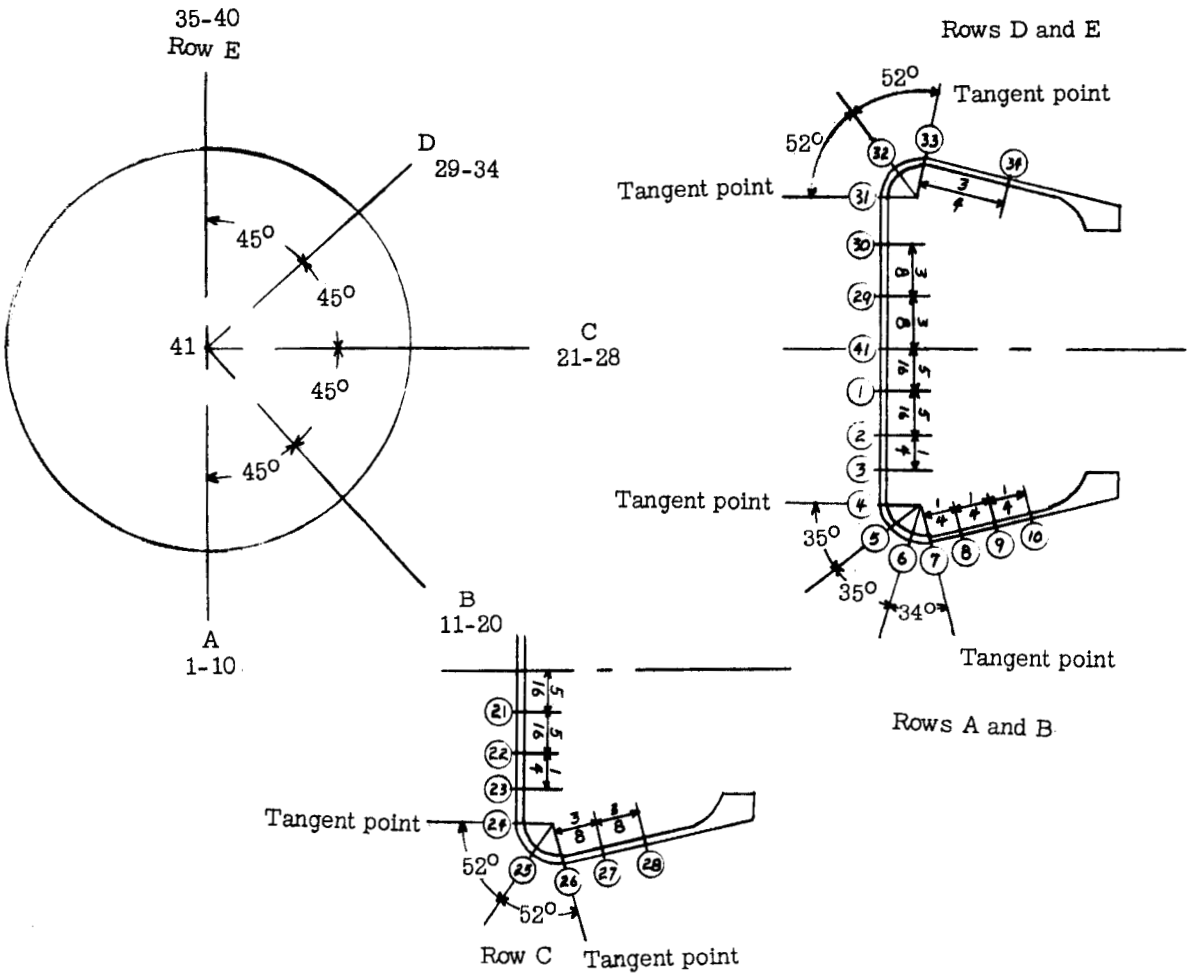

(a) Body.

Figure 4.- Thermocouple and pressure-orifice locations. All dimensions are in inches unless otherwise indicated.

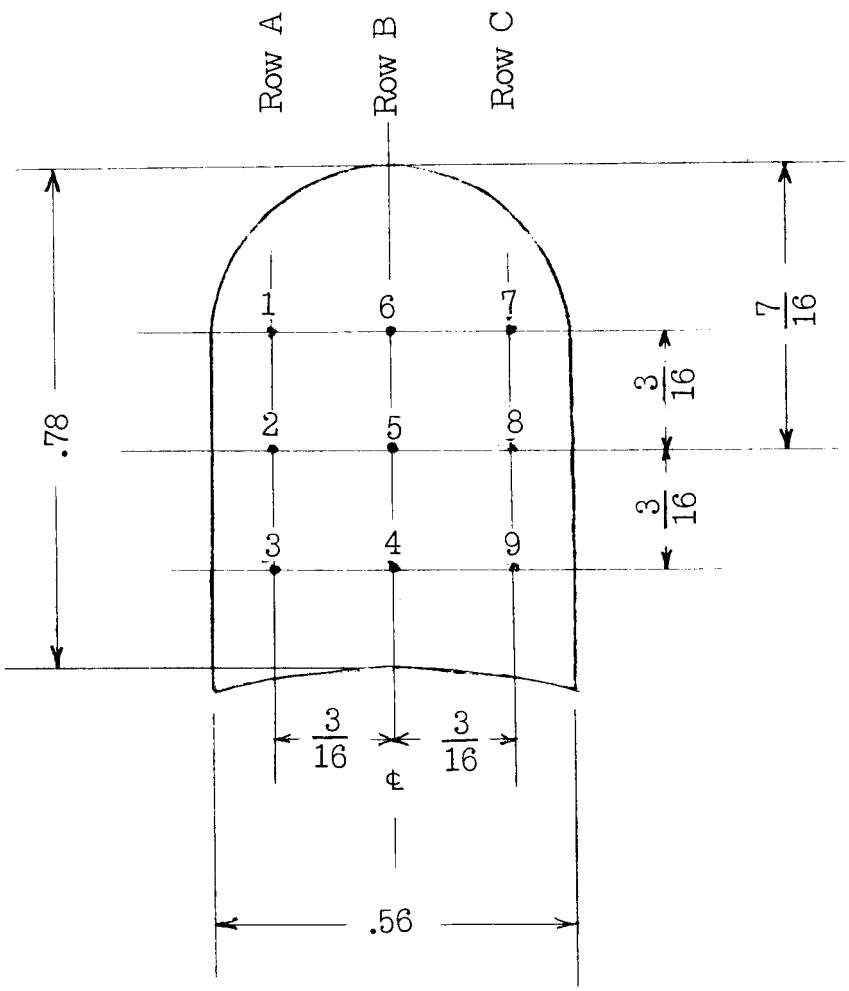

(b) Flap.

Figure 4.- Concluded.

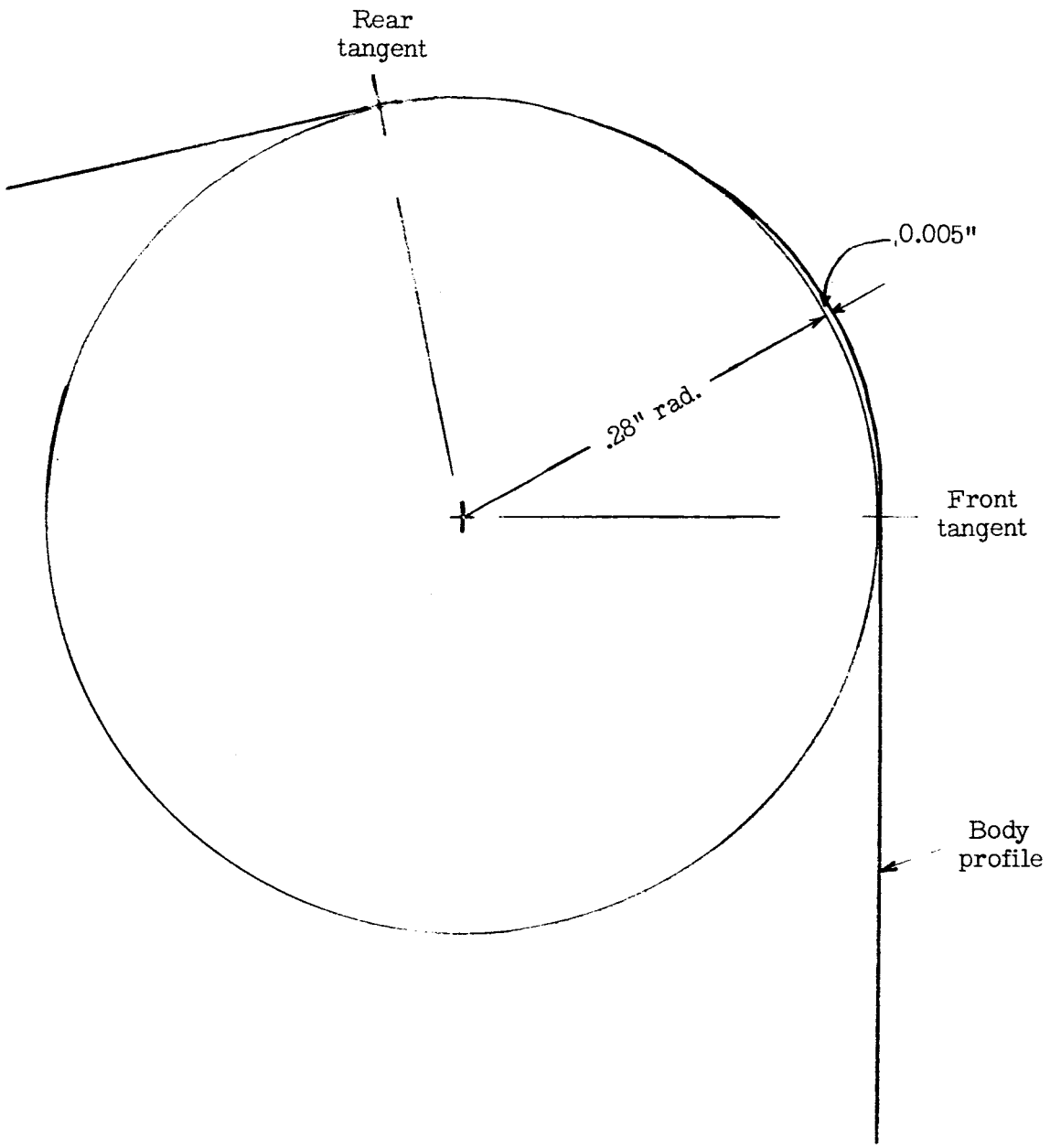

Figure 5.- Corner profile (X10).

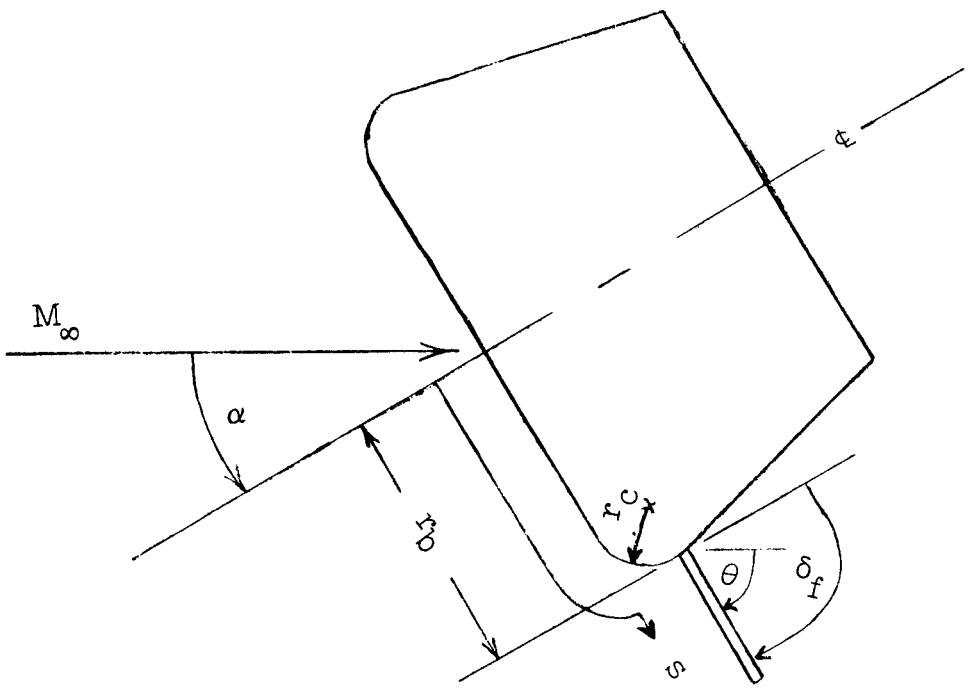

Figure 6.- Model orientation.

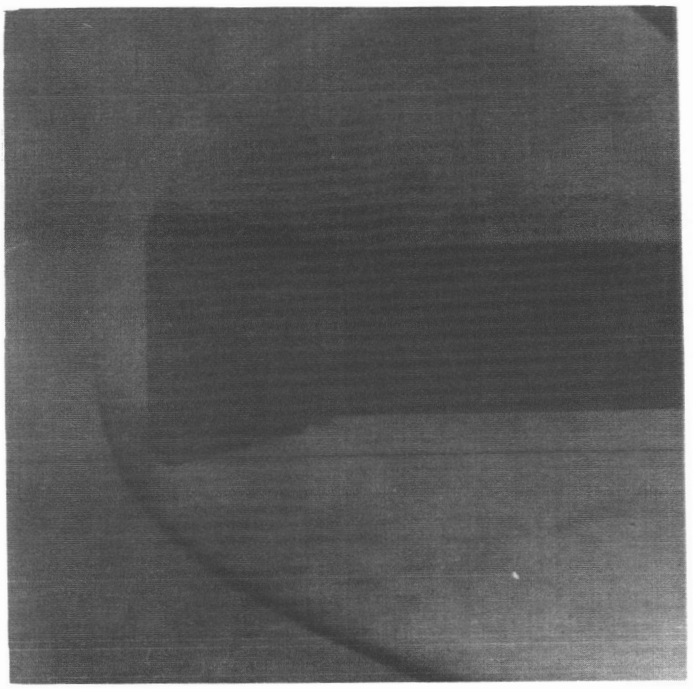

$\alpha = 0^{\circ}$

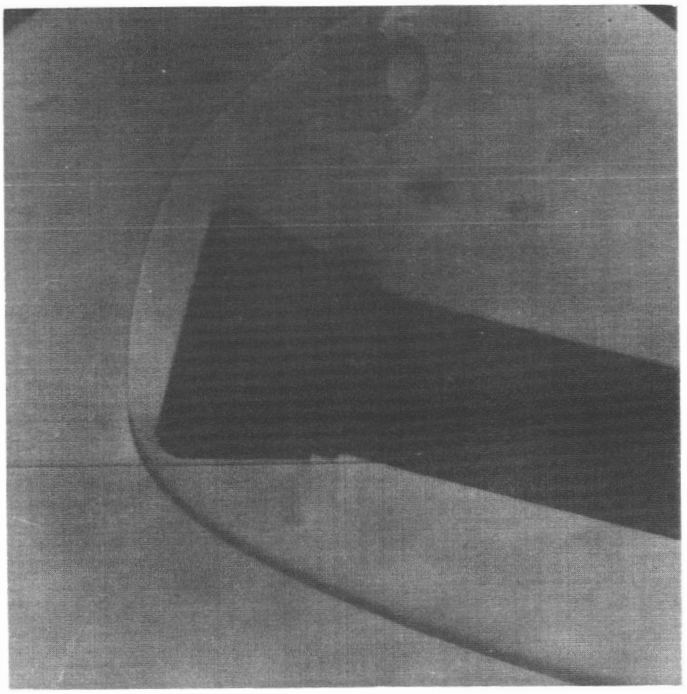

$\alpha = 15^{\circ}$

L-62-2080

Figure 7.- Schlieren photographs of flow about body.

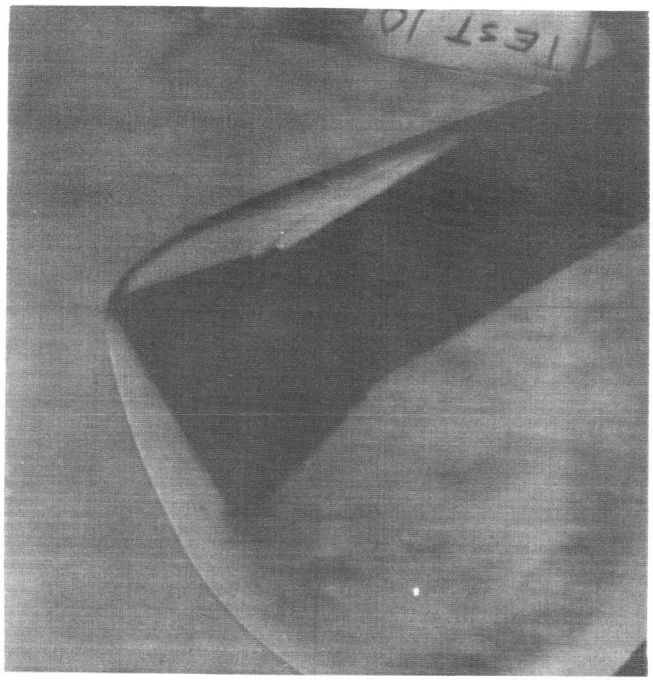

$\alpha = 30^{\circ}$

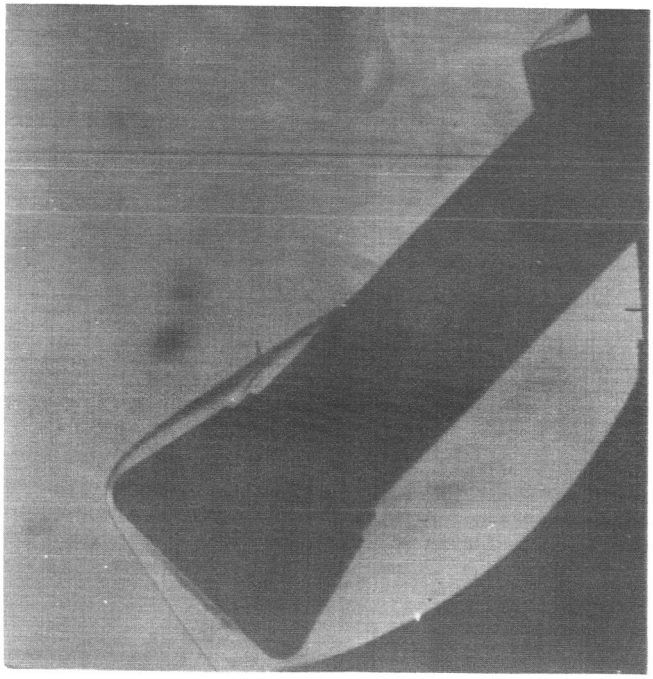

$\alpha = 45^{\circ}$

Figure 7.- Concluded. L-62-2081

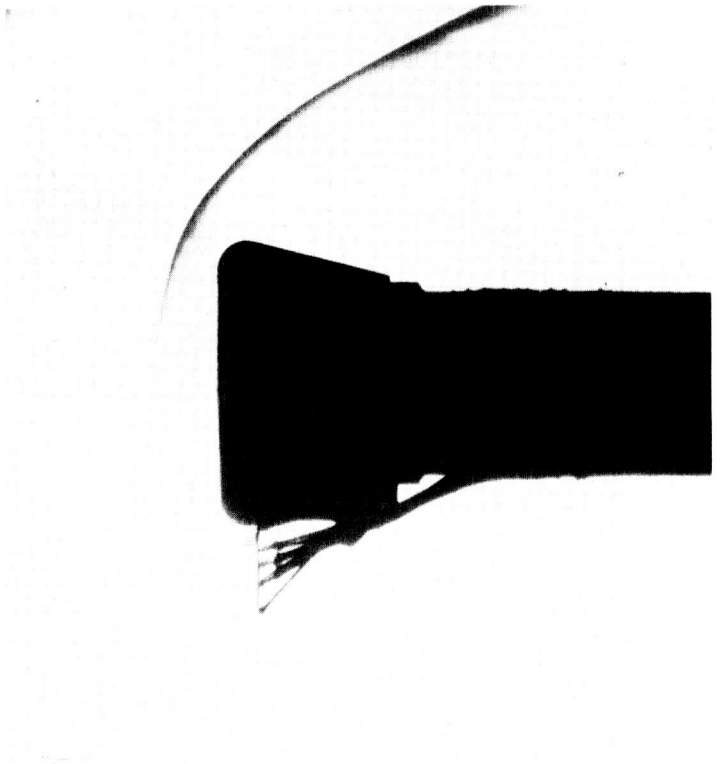

$\alpha = 0^{\circ}$

$\alpha = 15^{\circ}$

Figure 8.- Schlieren photographs of flow about leeward flap. $\delta_f = 90^{\circ}$. L-62-2082

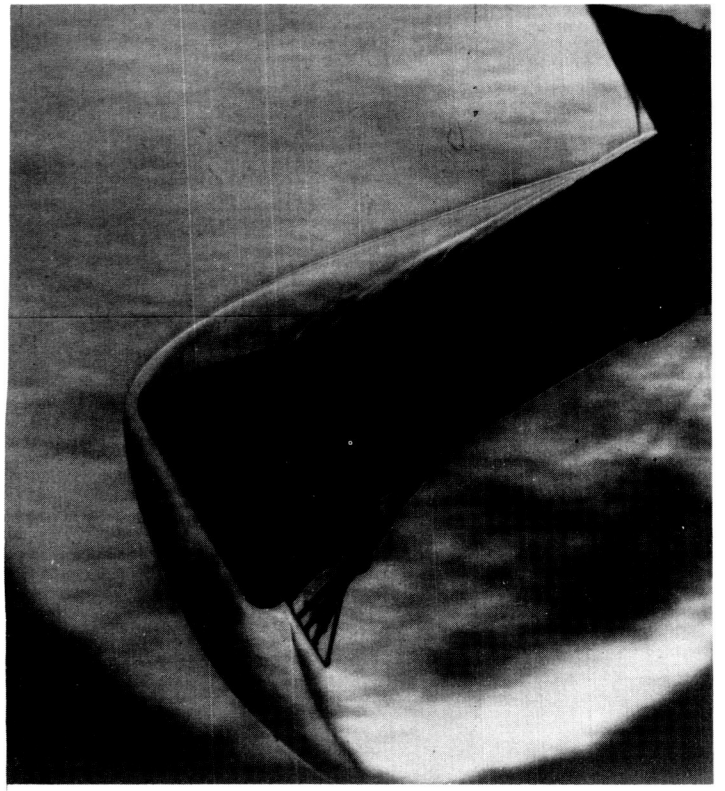

$\alpha = 30^{\circ}$

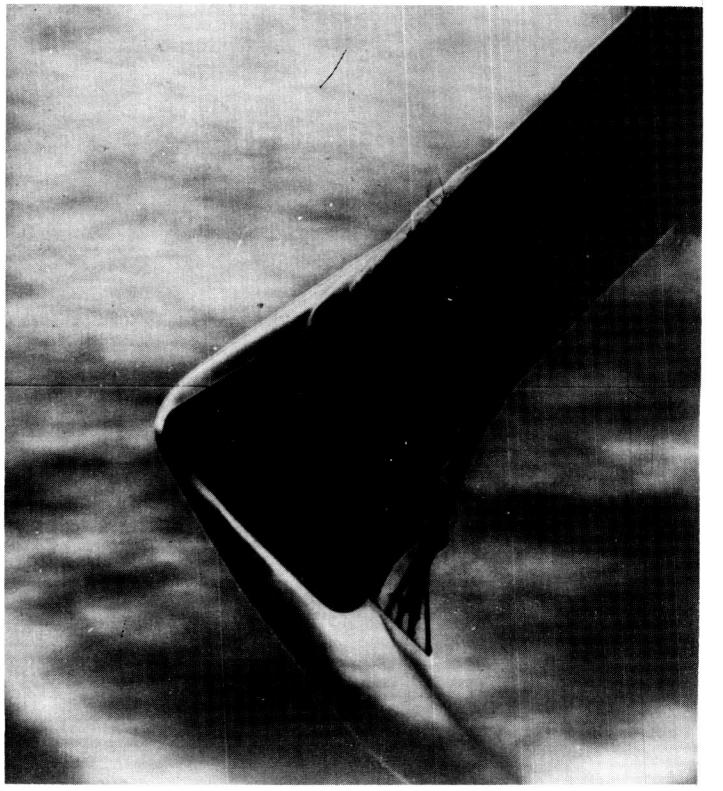

$\alpha = 45^{\circ}$

Figure 8.- Concluded. L-62-2083

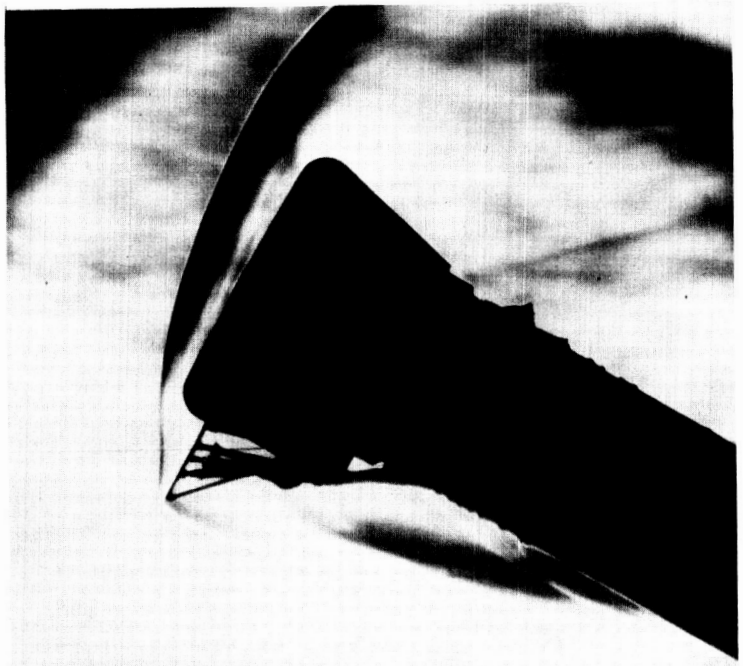

$\alpha = 30^{\circ}$

$\alpha = 45^{\circ}$

Figure 9.- Schlieren photographs of flow about windward flap. $\delta_f = 90^{\circ}$. L-62-2084

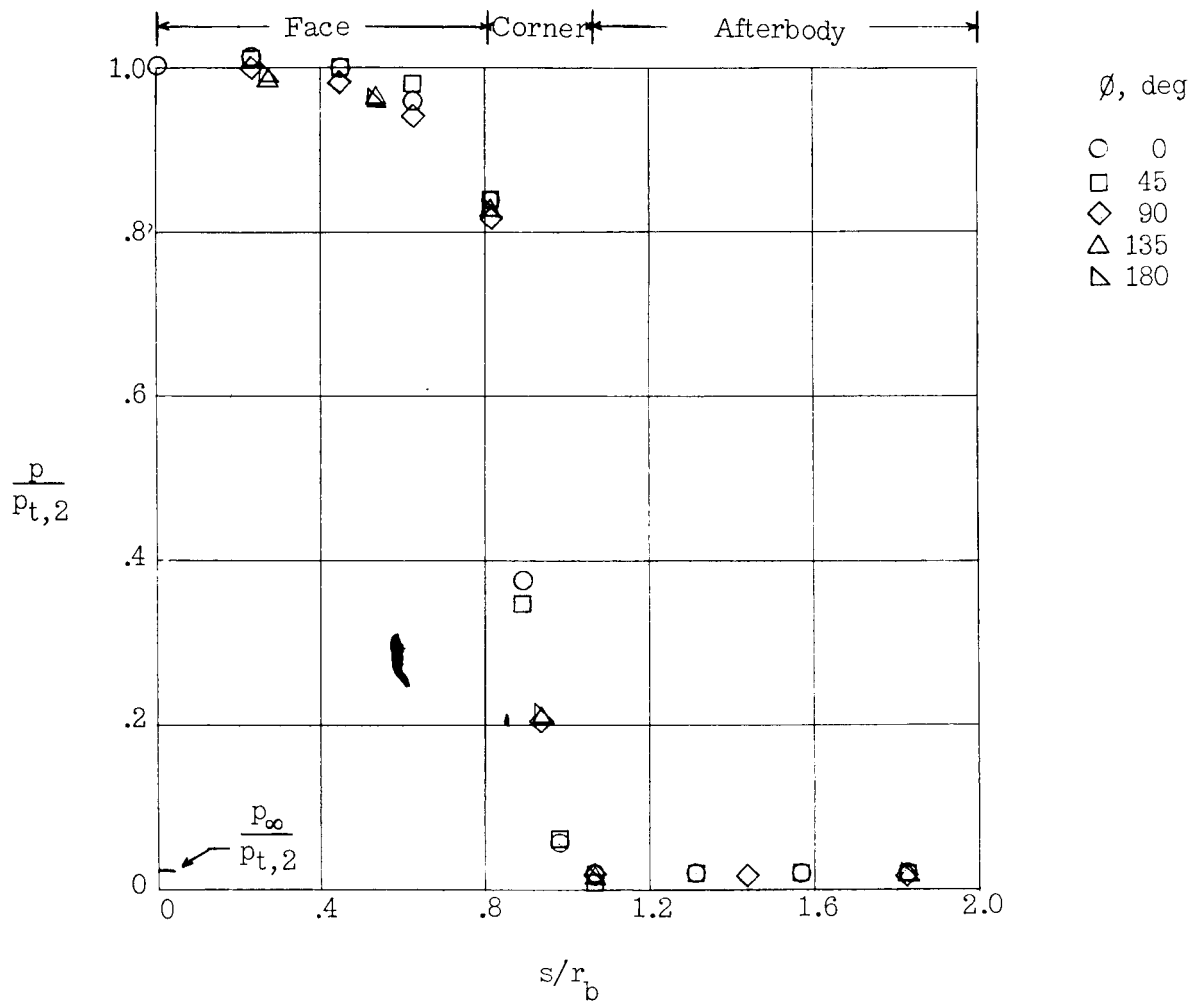

(a) $\alpha = 0^\circ$.

Figure 10.- Body pressure distribution. $R_\infty = 0.93 \times 10^6$.

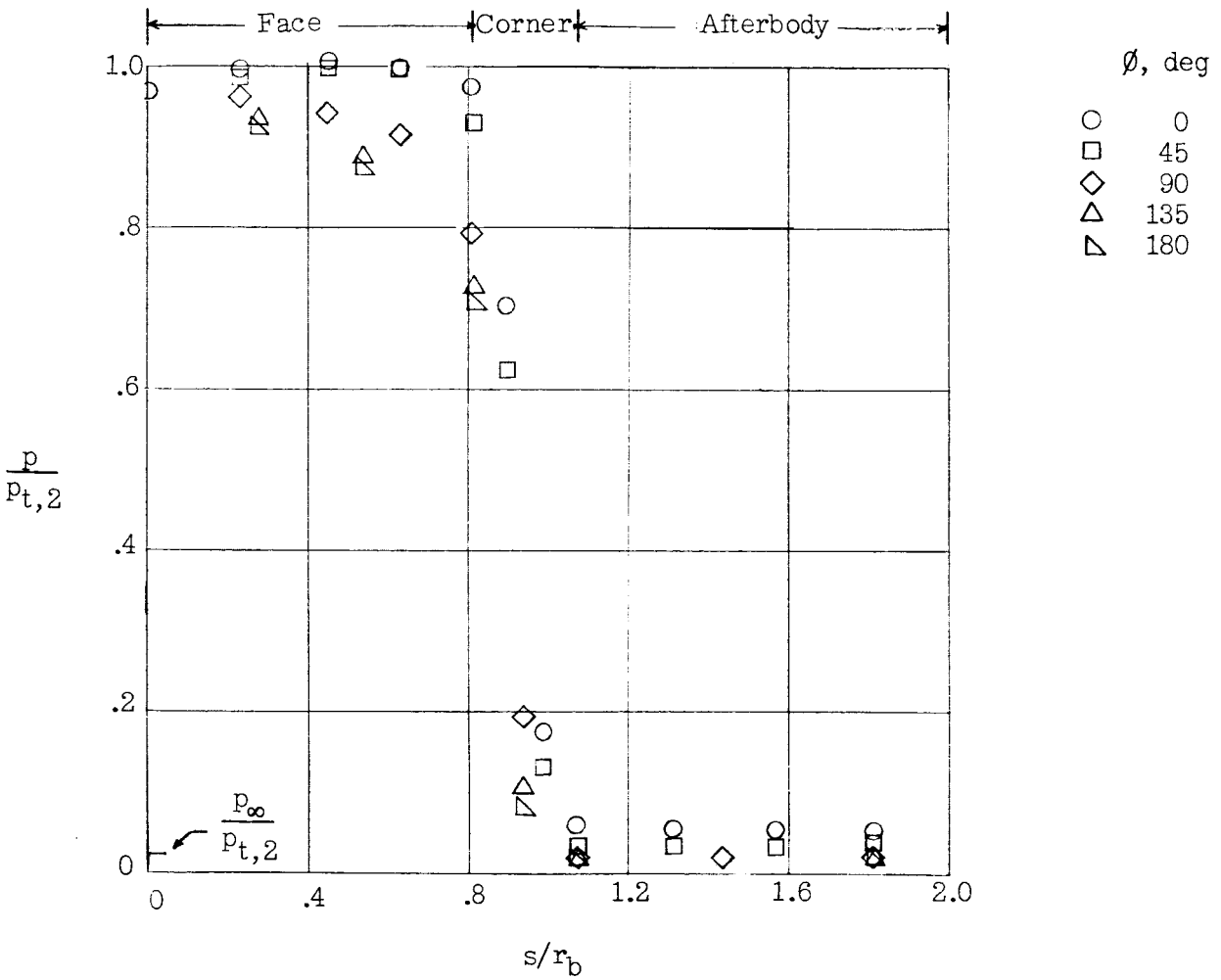

(b) $\alpha = 15^{\circ}$.

Figure 10.- Continued.

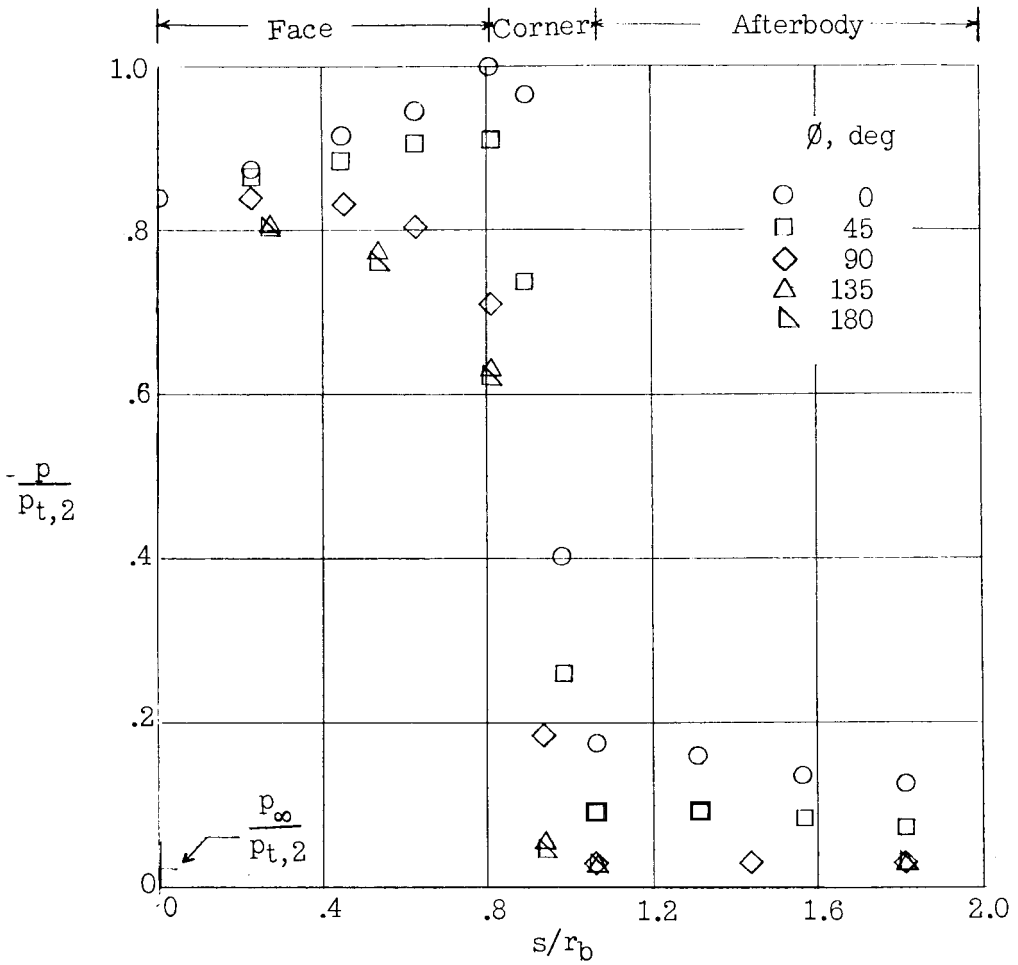

(c) $\alpha = 30^\circ$.

Figure 10.- Continued.

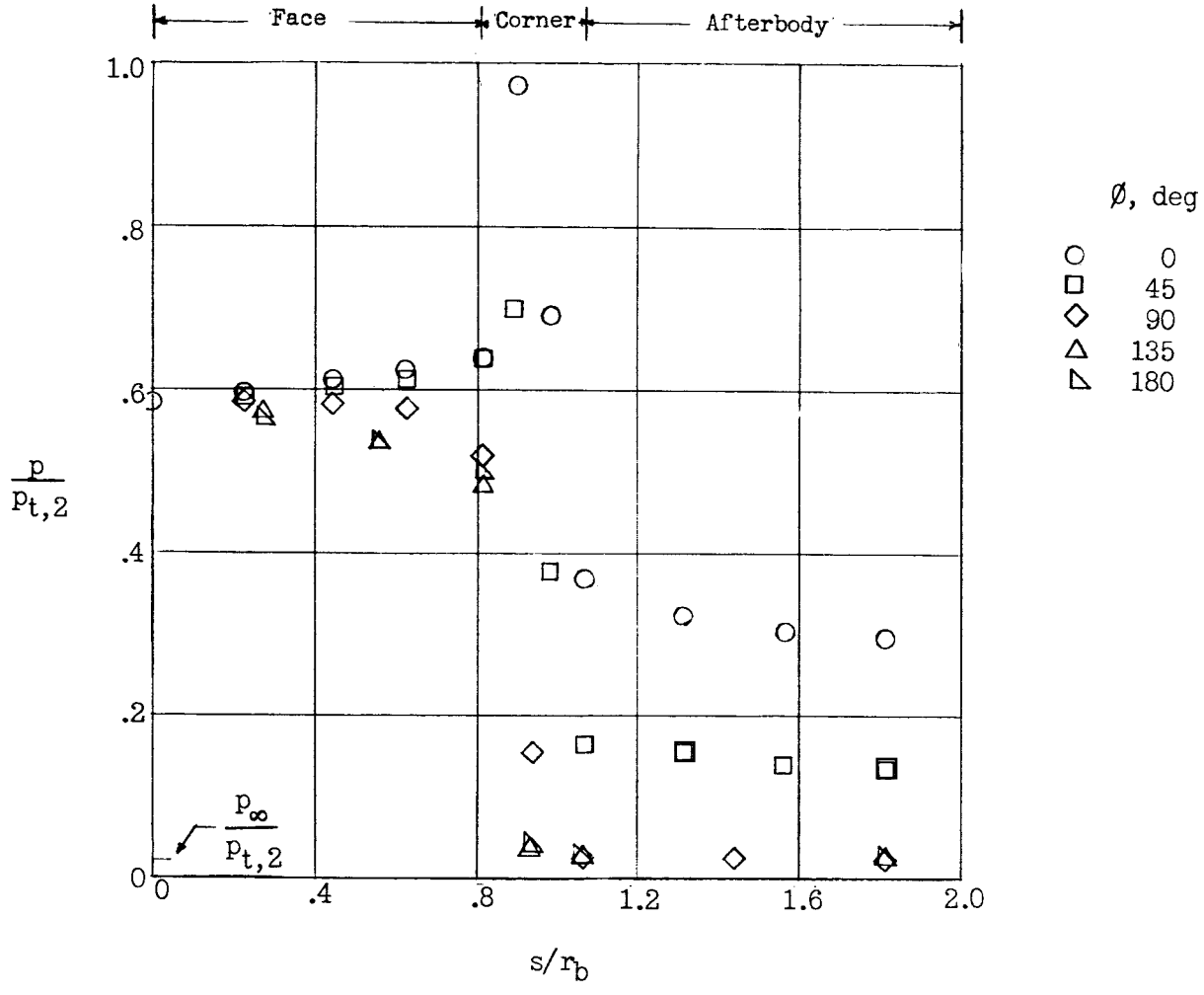

(d) $\alpha = 45^\circ$.

Figure 10.- Concluded.

[redacted]

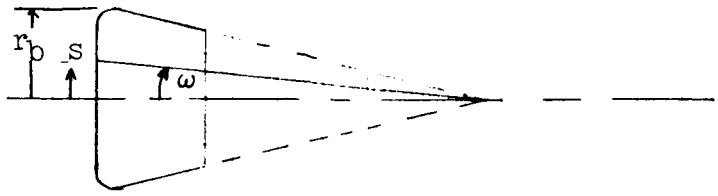

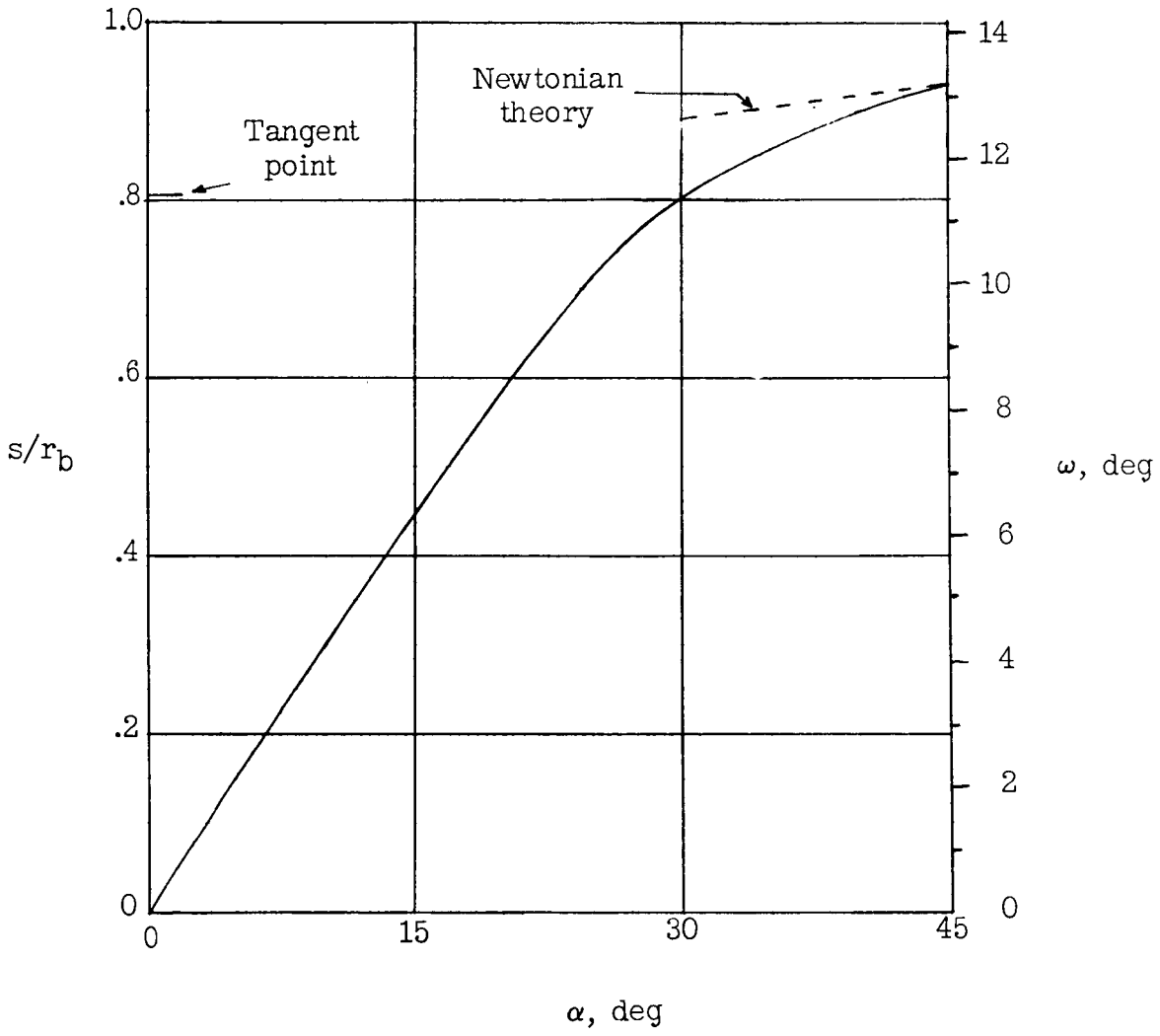

Figure 11.- Movement of stagnation point with angle of attack. (Stagnation-point location was determined within $\pm 0.05 s/r_b$.)

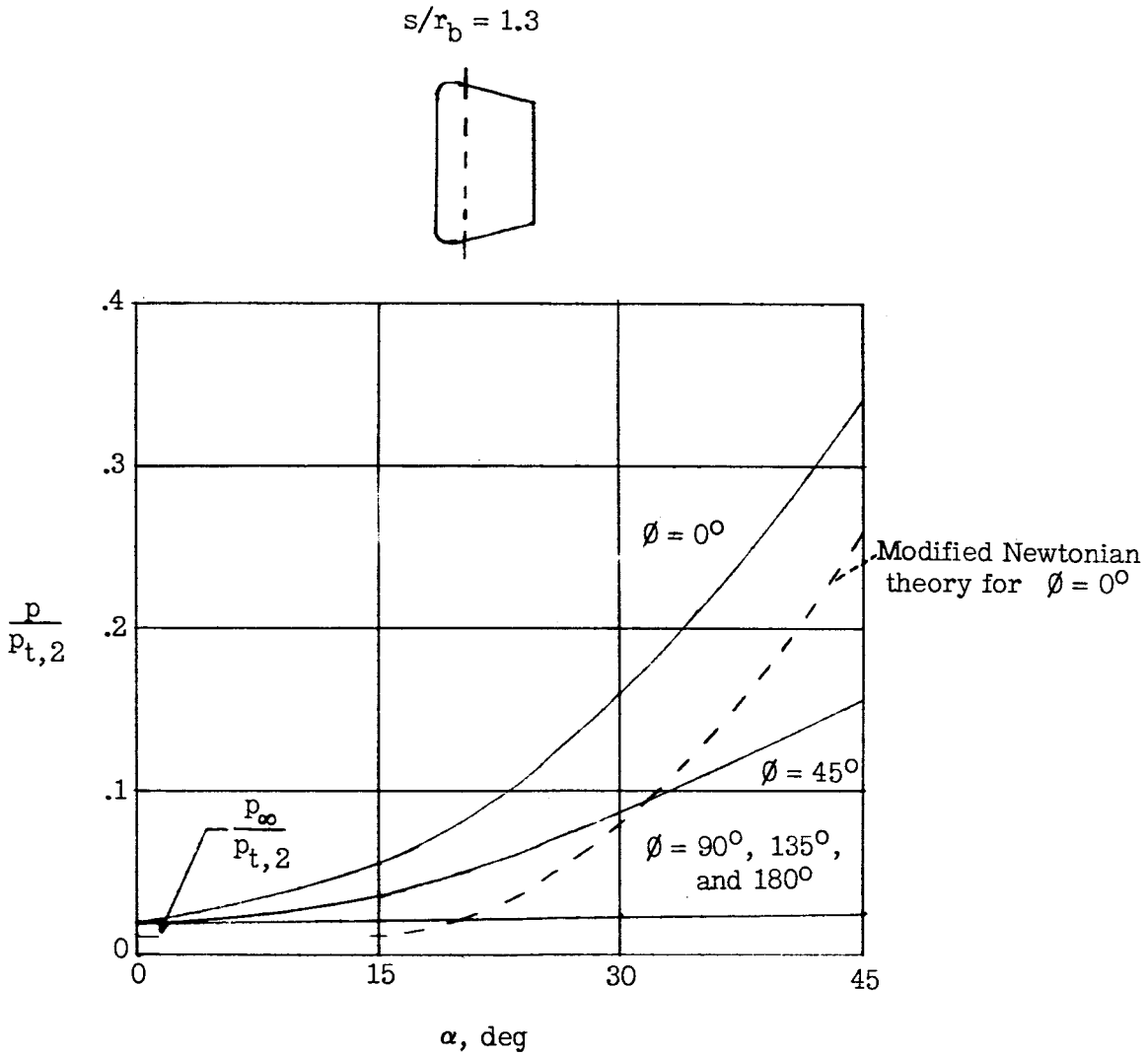

Figure 12.- Variation of faired afterbody pressure with angle of attack. $s/r_b = 1.3$.

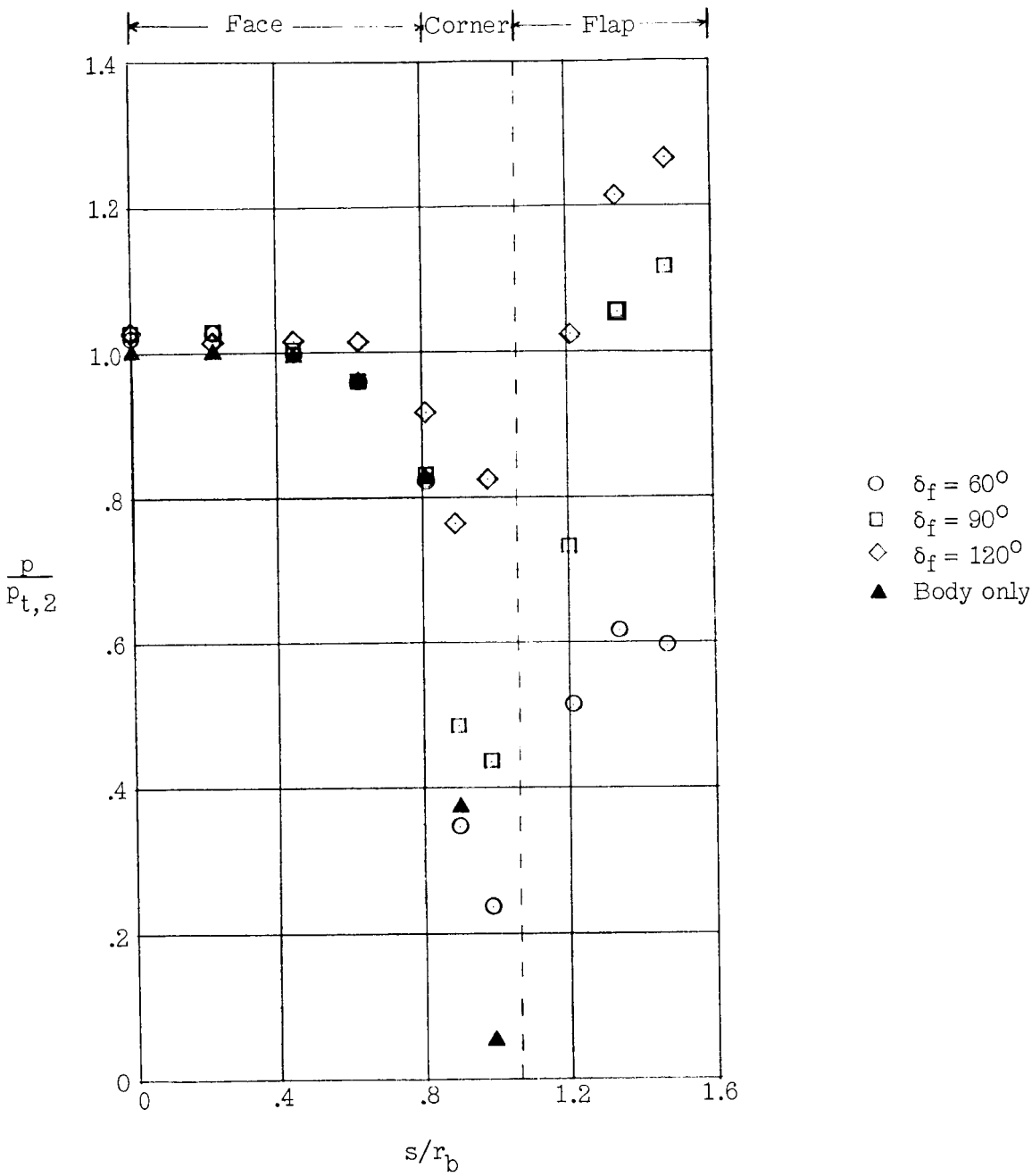

(a) $\alpha = 0^{\circ}$.

Figure 13.- Pressure distribution on body—leeward-flap configuration. (Windward ray; $R_{\infty} = 0.93 \times 10^{6}$.)

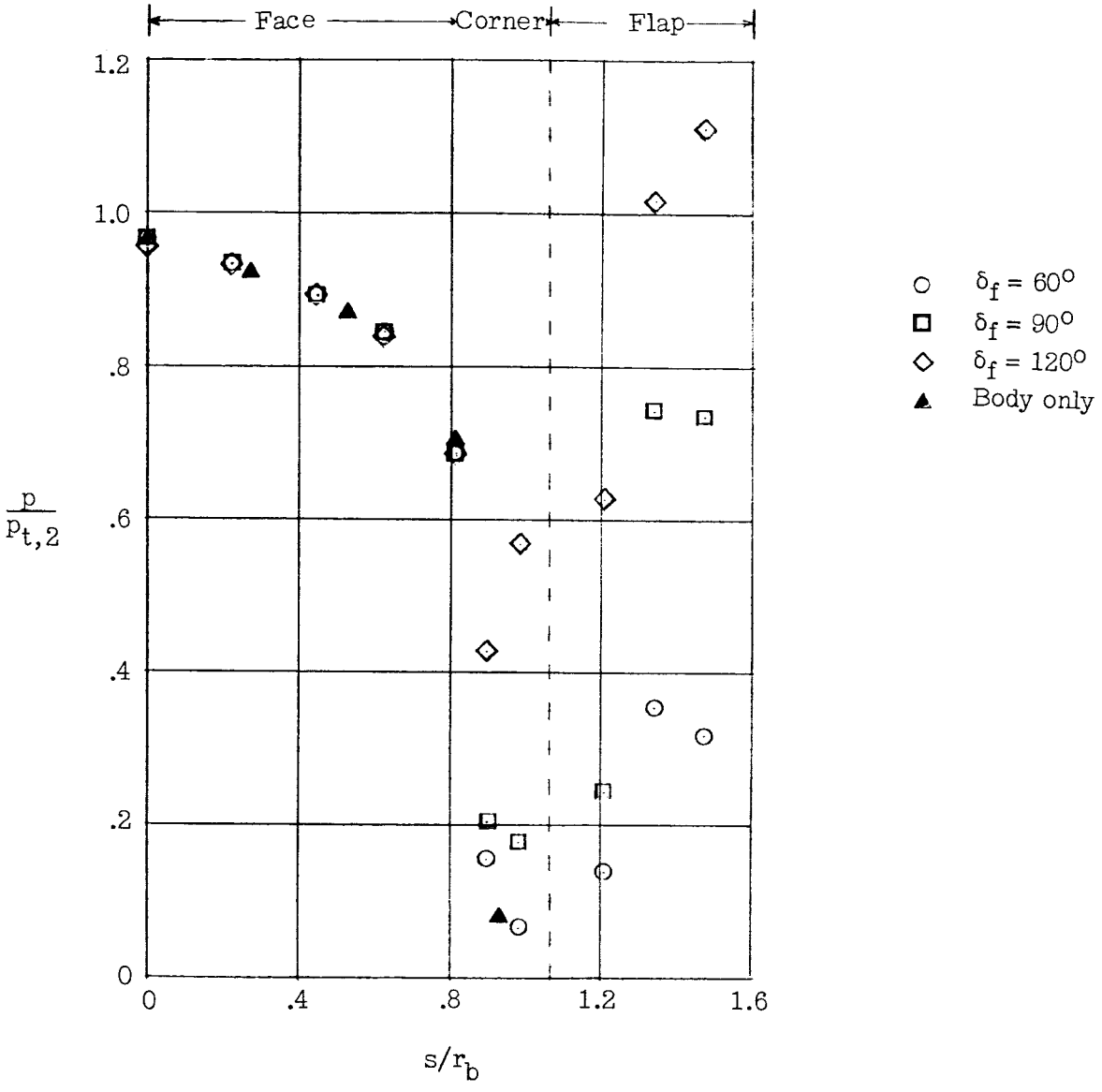

(b) $\alpha = 15^o$.

Figure 13.- Continued.

[redacted]

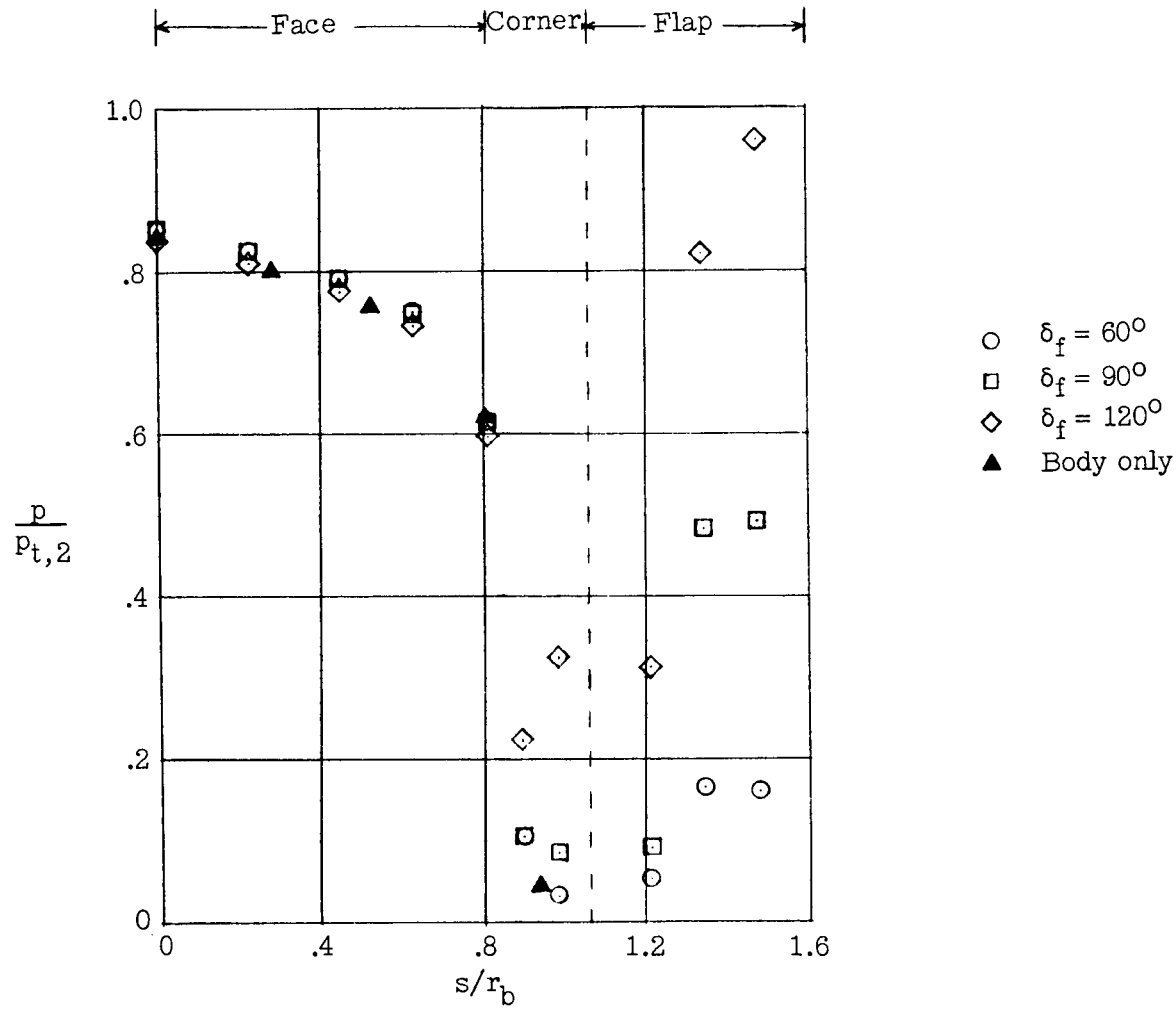

(c) $\alpha = 30^\circ$.

Figure 13.- Continued.

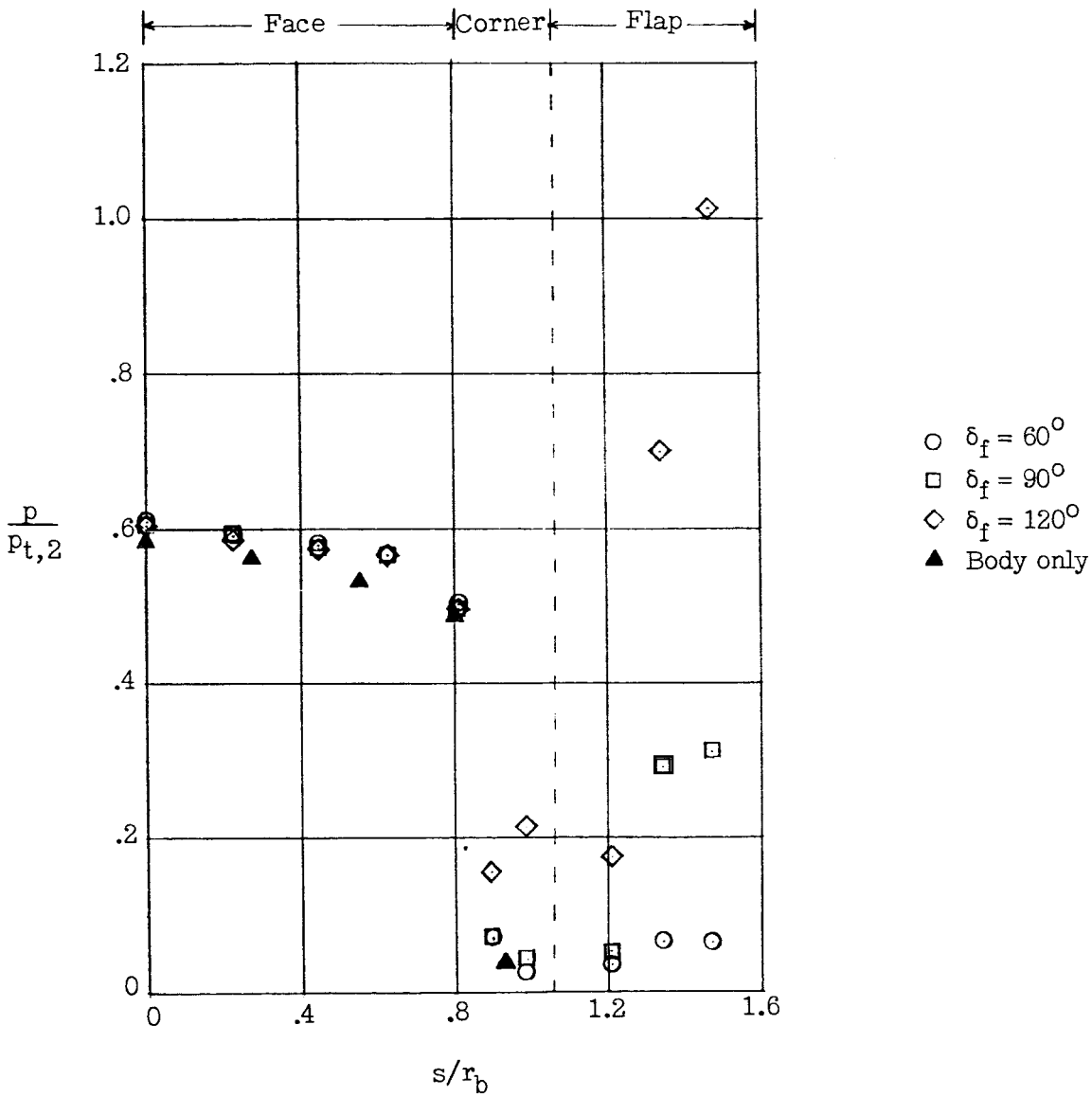

(d) $\alpha = 45^{\circ}$.

Figure 13.- Concluded.

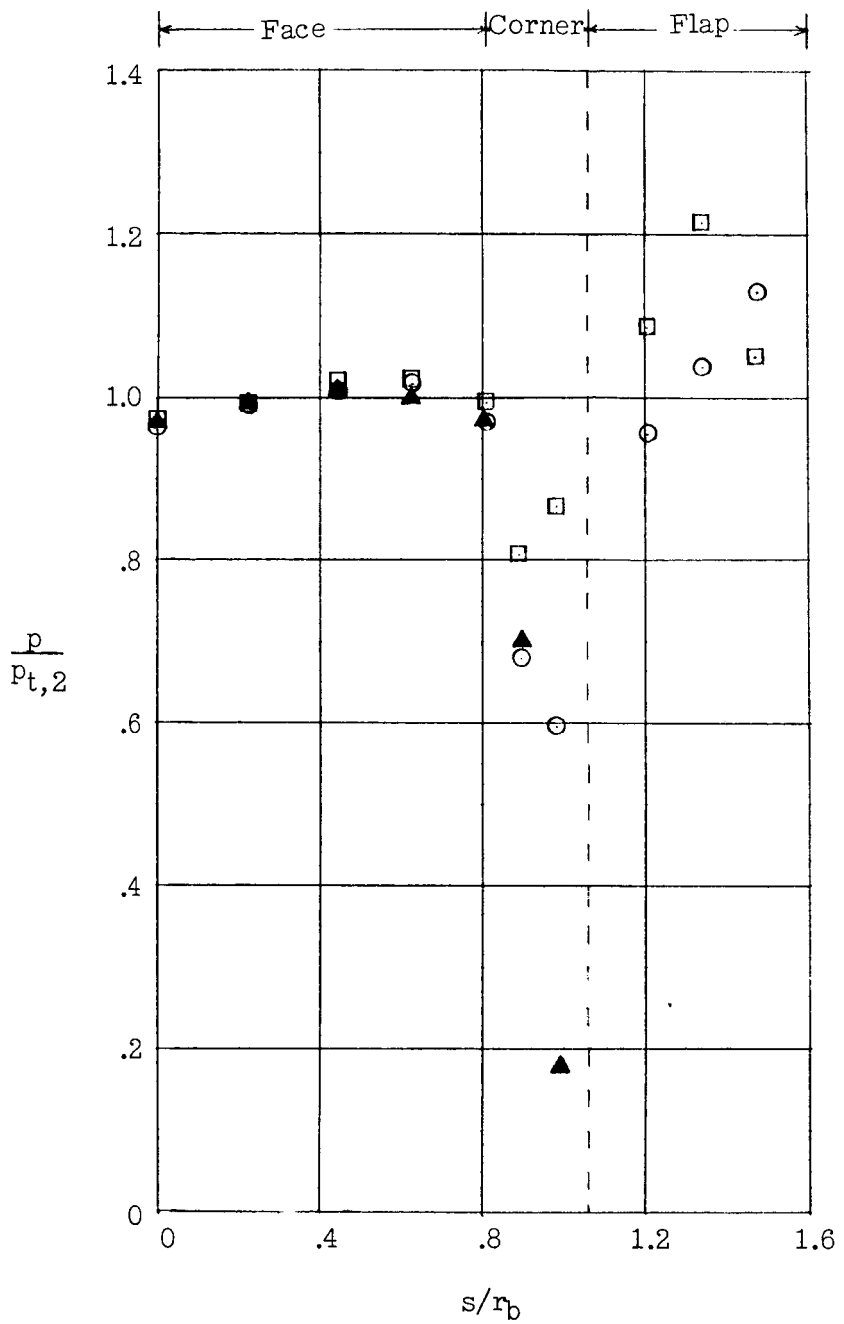

(a) $\alpha = 15^{\circ}$.

Figure 14.- Pressure distributions on body—windward-flap configuration. (Windward ray; $R_{\infty} = 0.93 \times 10^{6}$.)

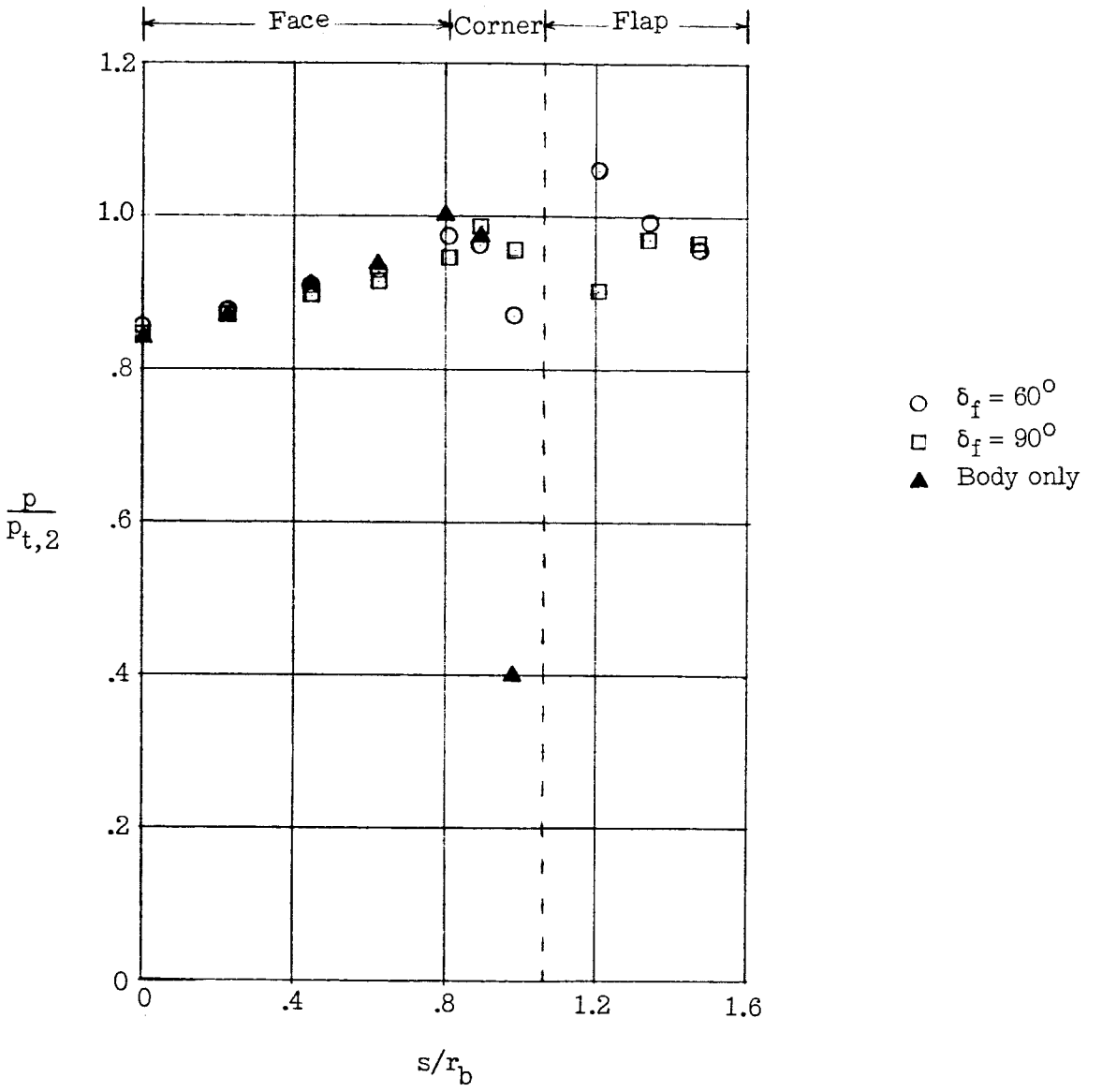

(b) $\alpha = 30^\circ$.

Figure 14.- Continued.

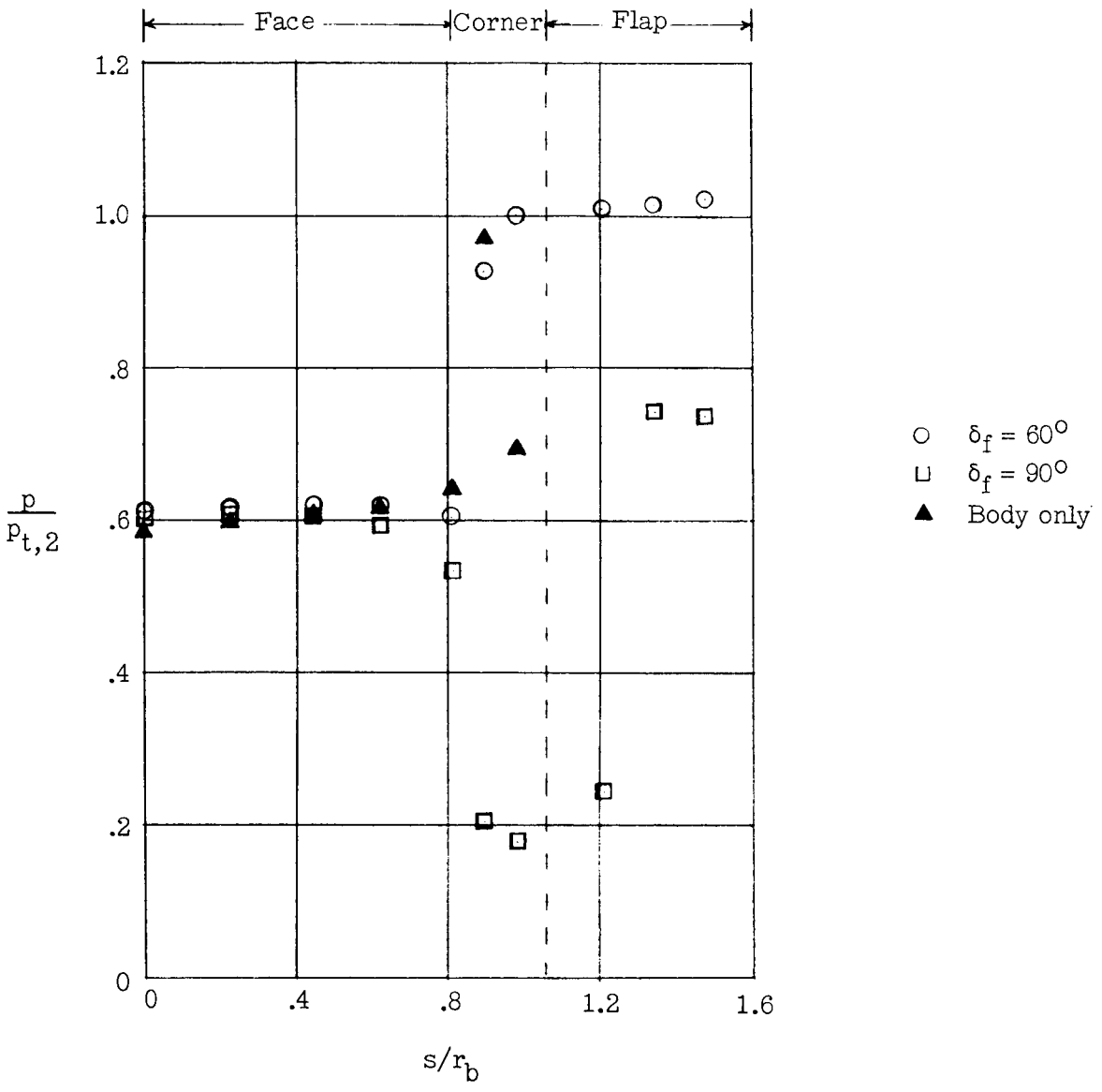

(c) $\alpha = 45^\circ$.

Figure 14.- Concluded.

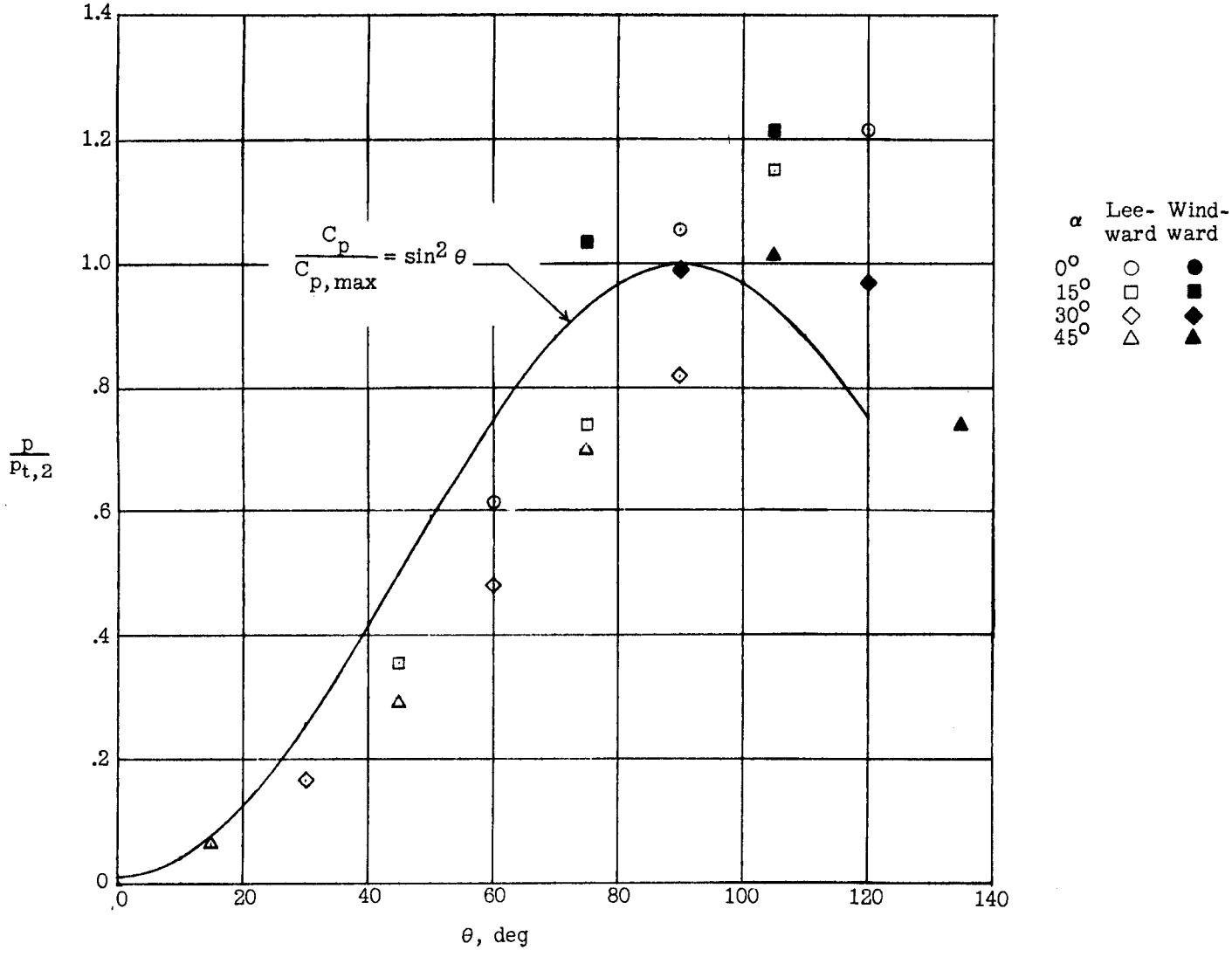

Figure 15.- Variation of flap pressure with flap angle.

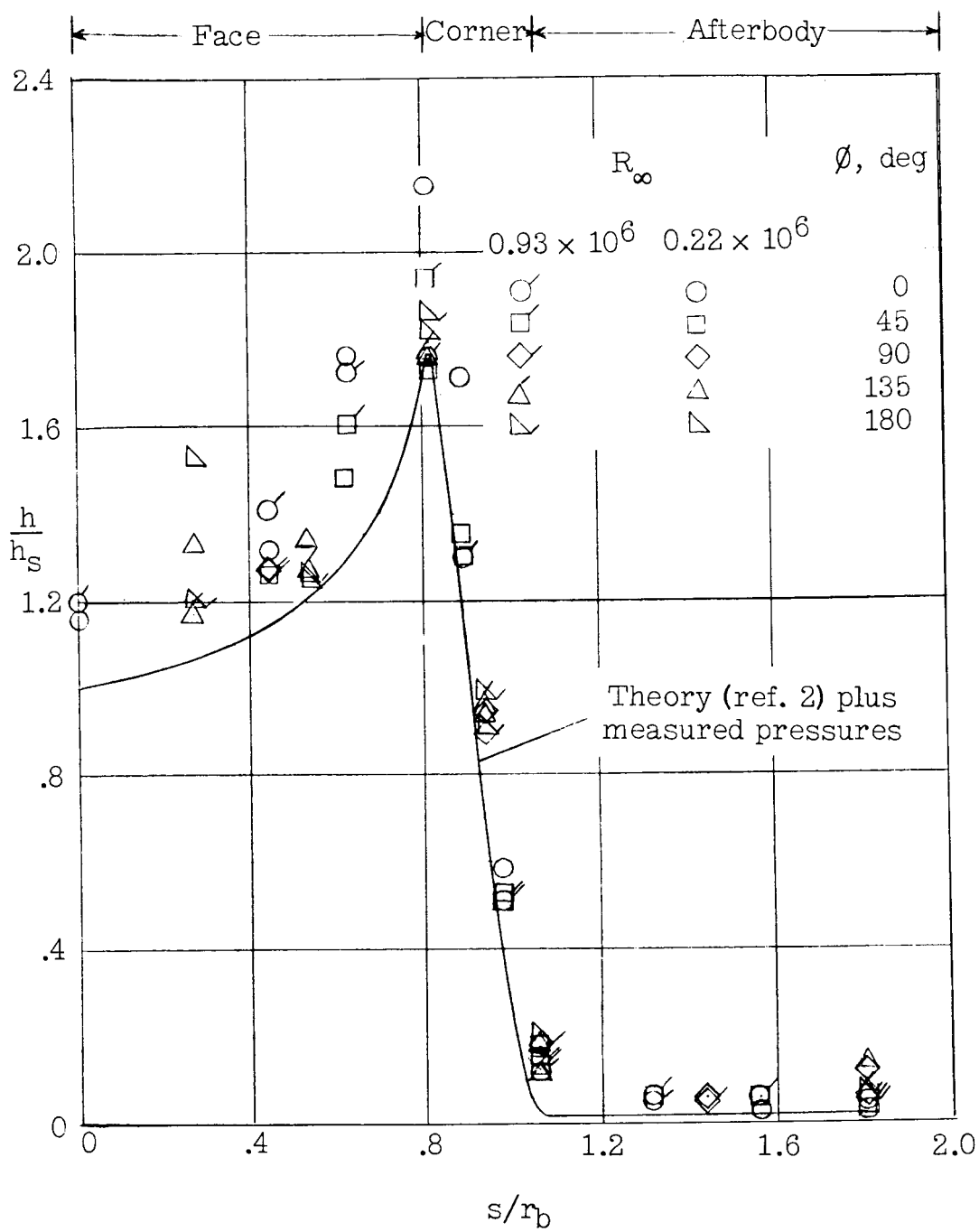

(a) $\alpha = 0^\circ$.

Figure 16.- Body heat-transfer distribution.

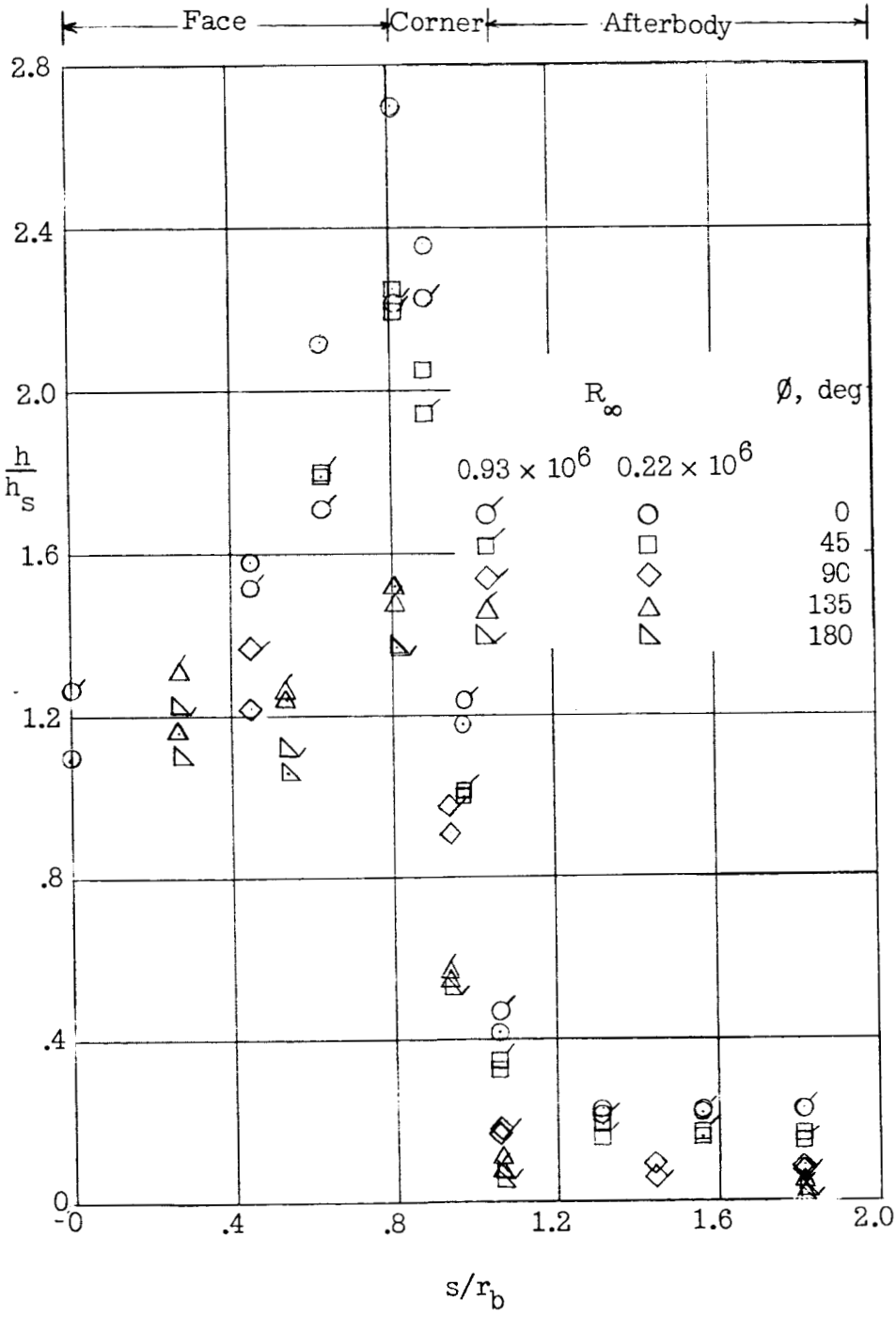

(b) $\alpha = 15^{\circ}$.

Figure 16.- Continued.

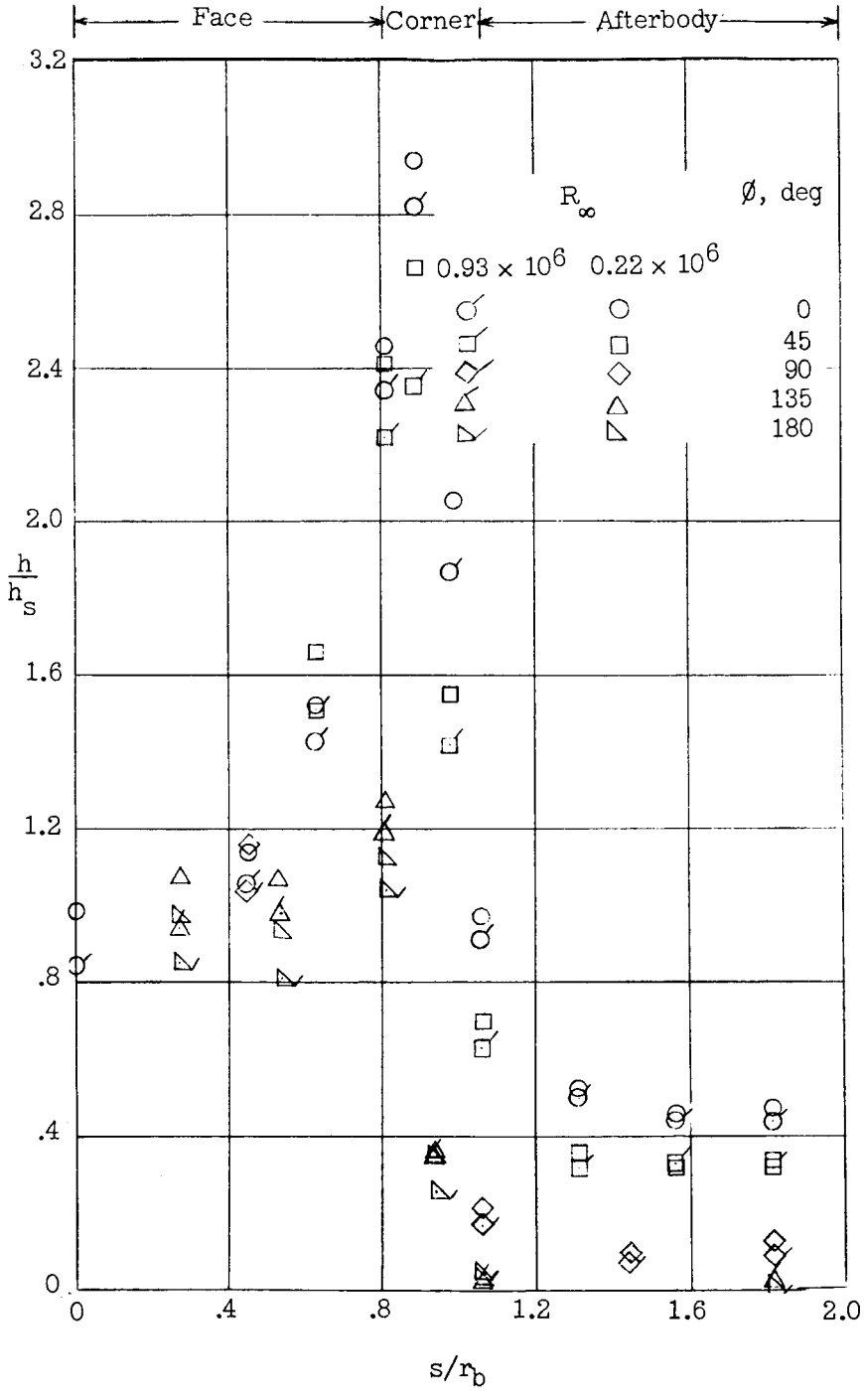

(c) $\alpha = 30^\circ$.

Figure 16.- Continued.

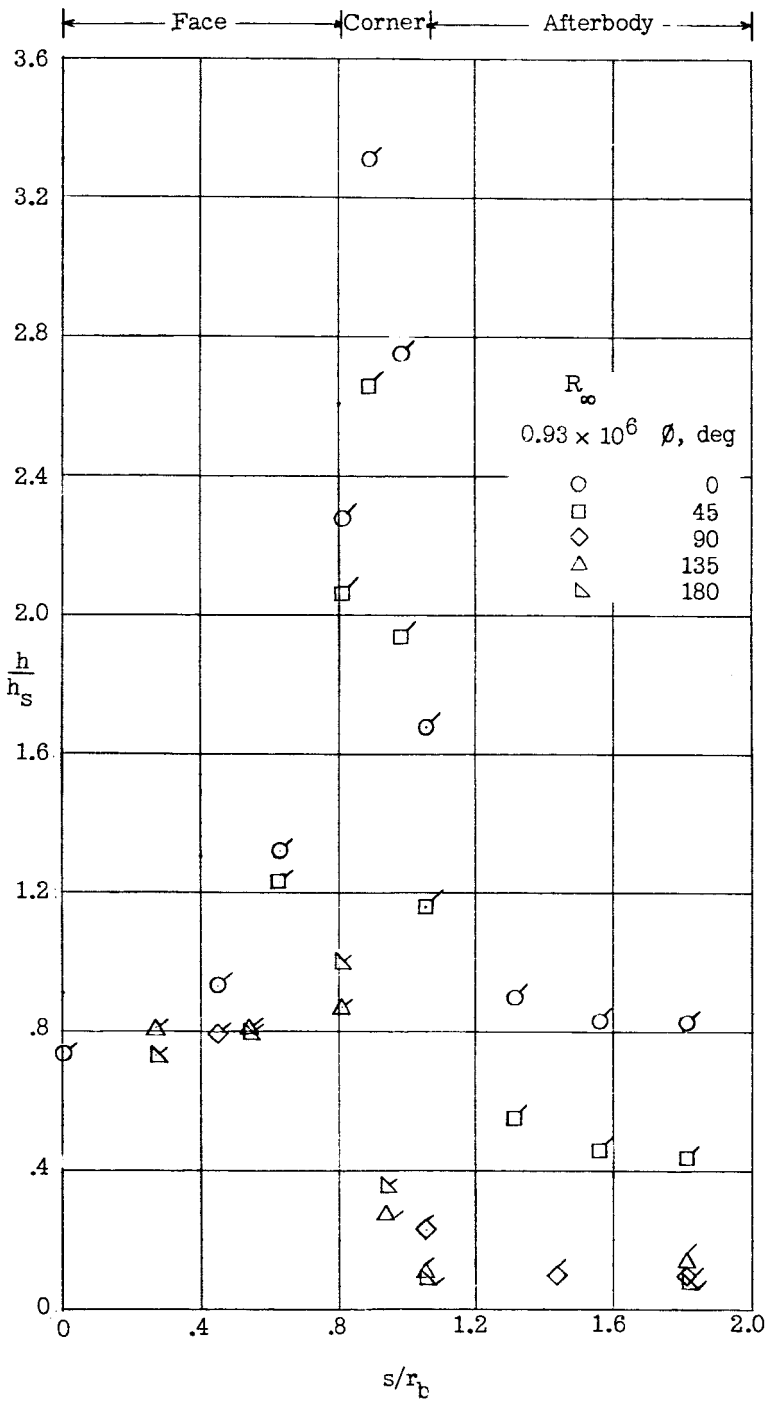

(d) $\alpha = 45^\circ$.

Figure 16.- Concluded.

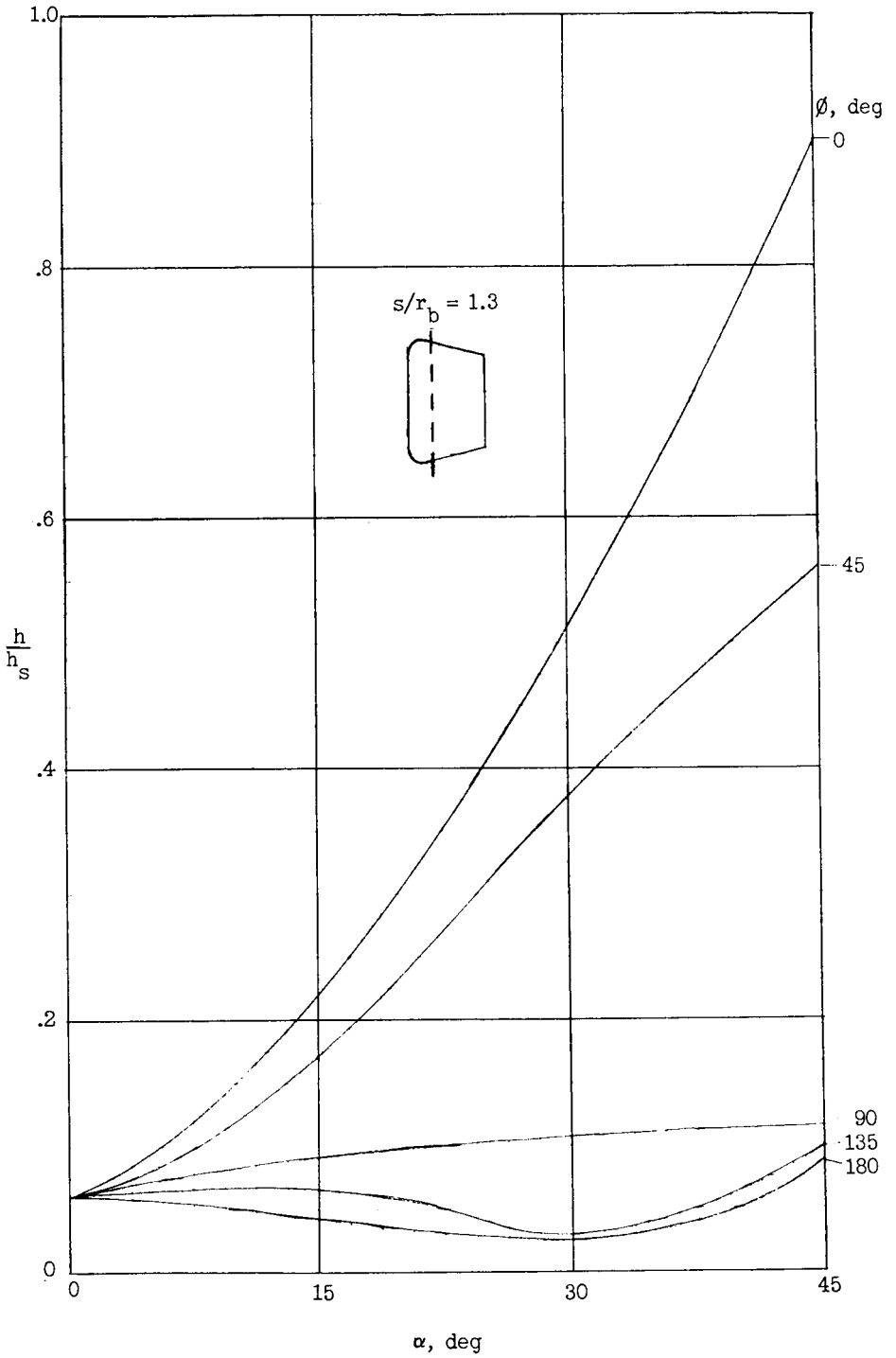

Figure 17.- Variation of afterbody heating with angle of attack. $s/r_b = 1.3$.

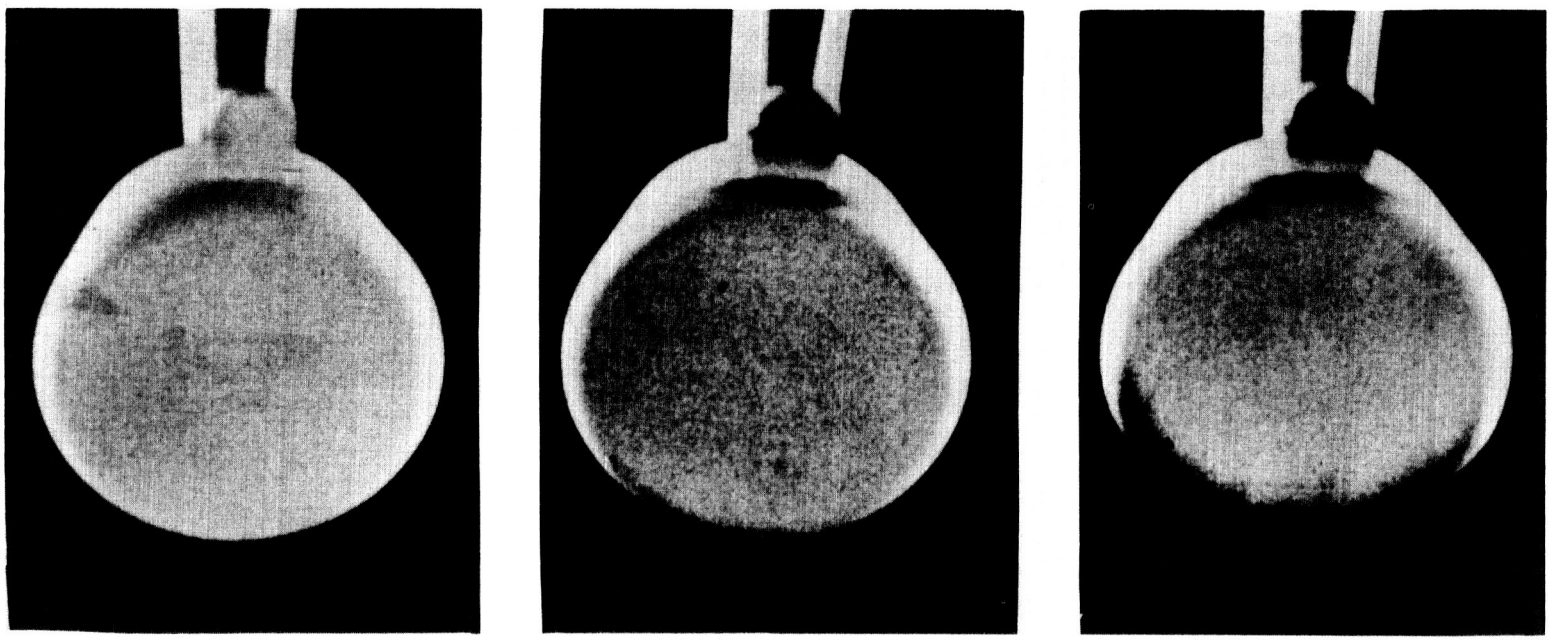

No flow Early time Late time

(a) Actual photographs. L-62-2085

Figure 18.- Results obtained with temperature-sensitive paint. $\alpha = 45^{\circ}$; $\delta_f = 120^{\circ}$; leeward flap.

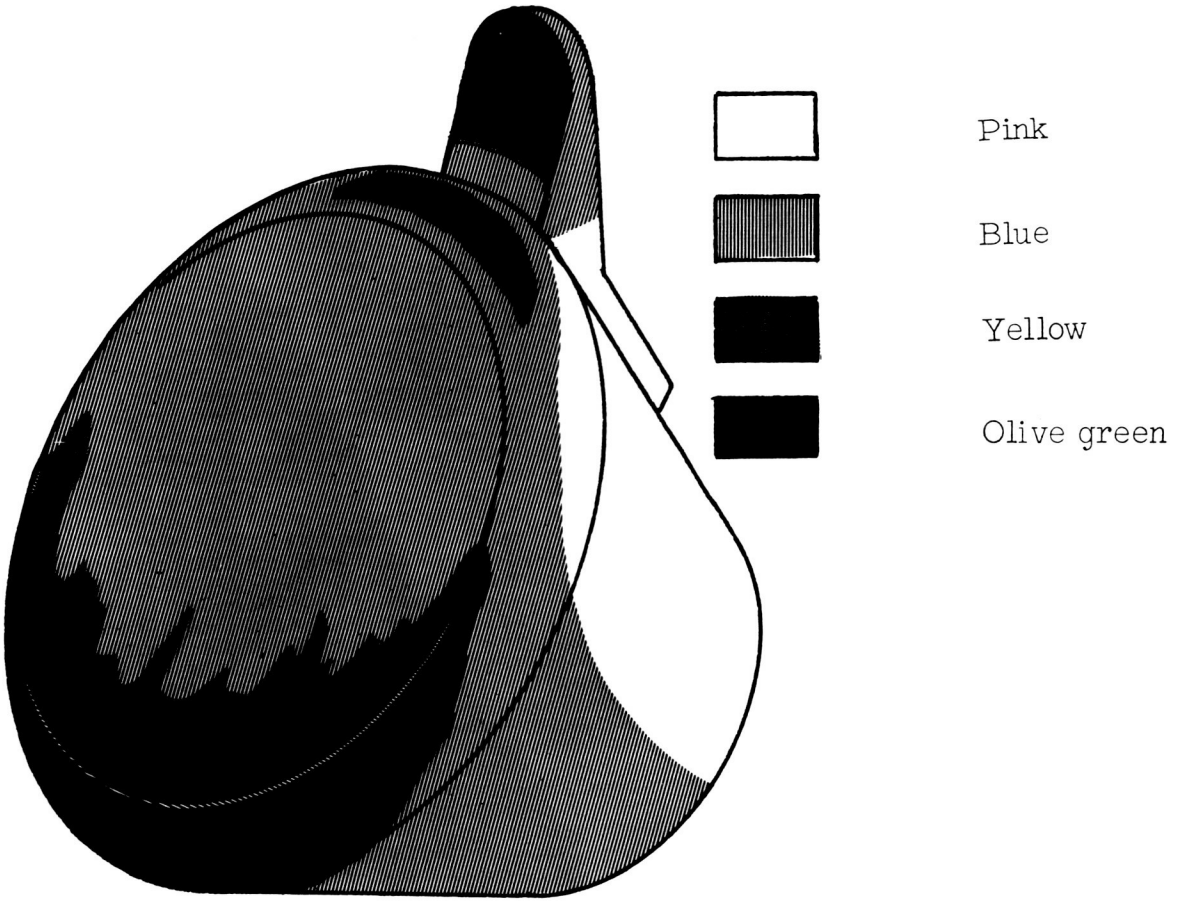

(b) Artist's sketch (late time).

Figure 18.- Concluded.

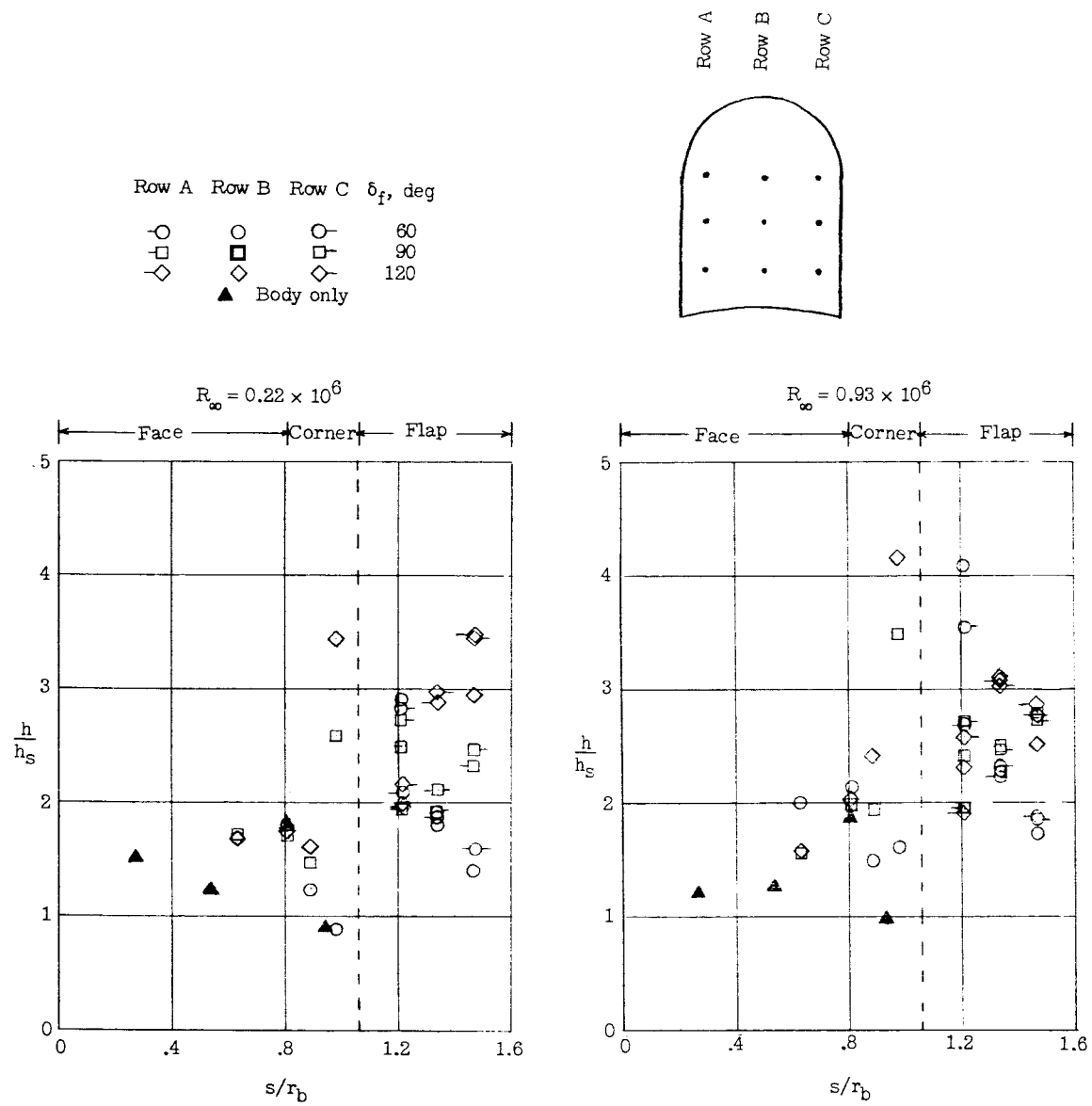

(a) $\alpha = 0^\circ$.

Figure 19.- Heat transfer to leeward flap.

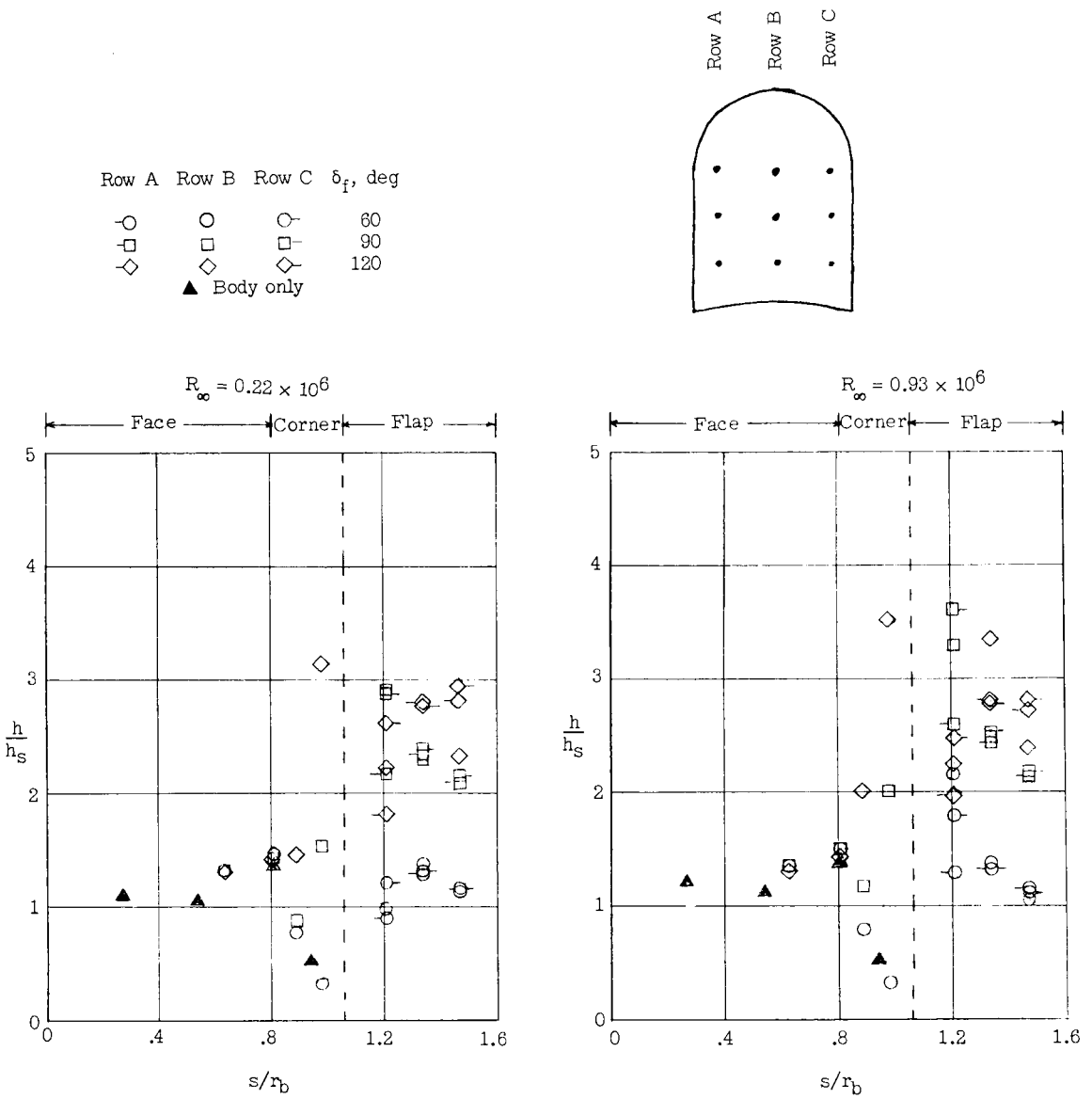

(b) $\alpha = 15^\circ$.

Figure 19.- Continued.

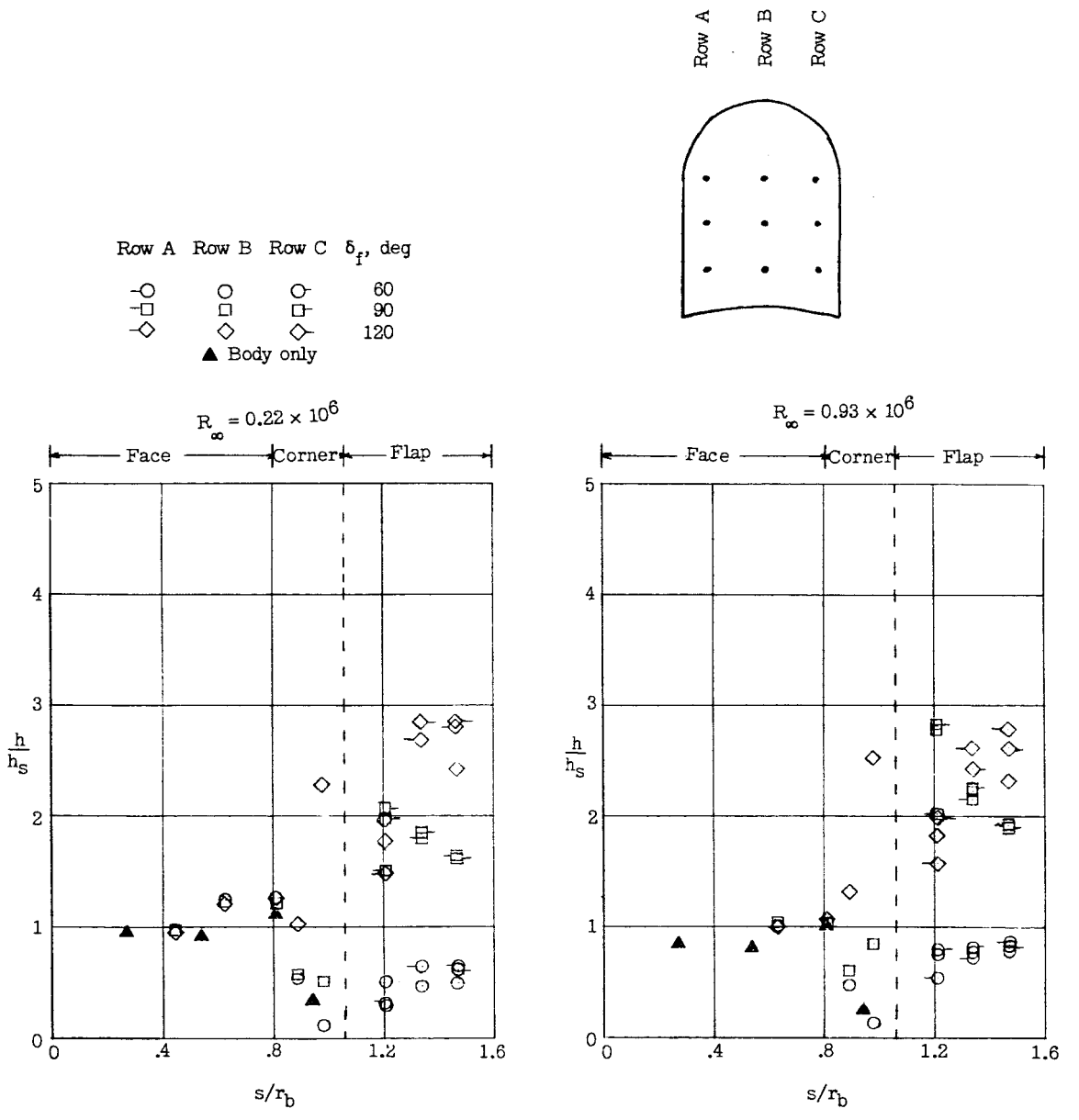

(c) $\alpha = 30^\circ$.

Figure 19.- Continued.

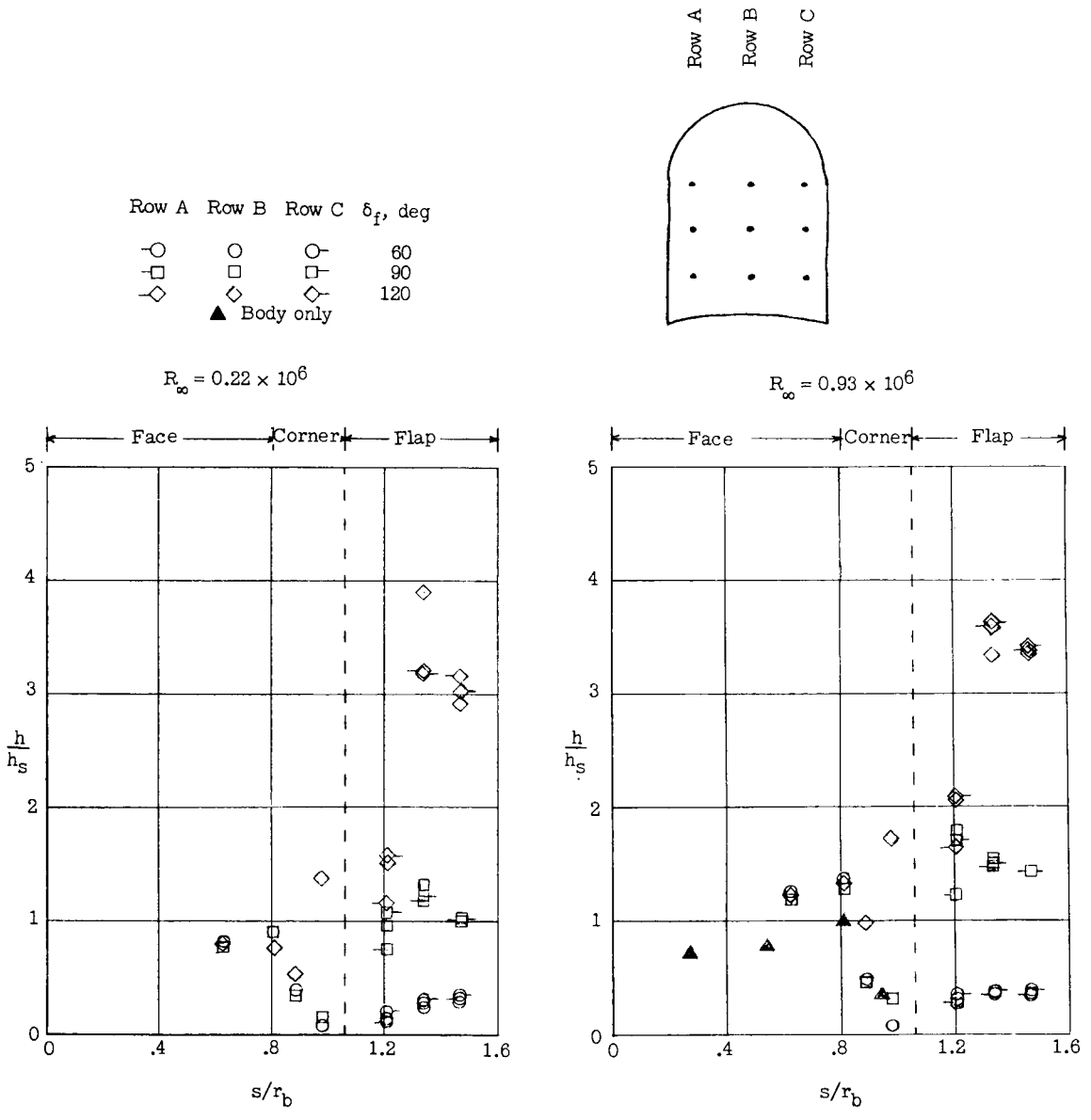

(d) $\alpha = 45°$.

Figure 19.- Concluded.

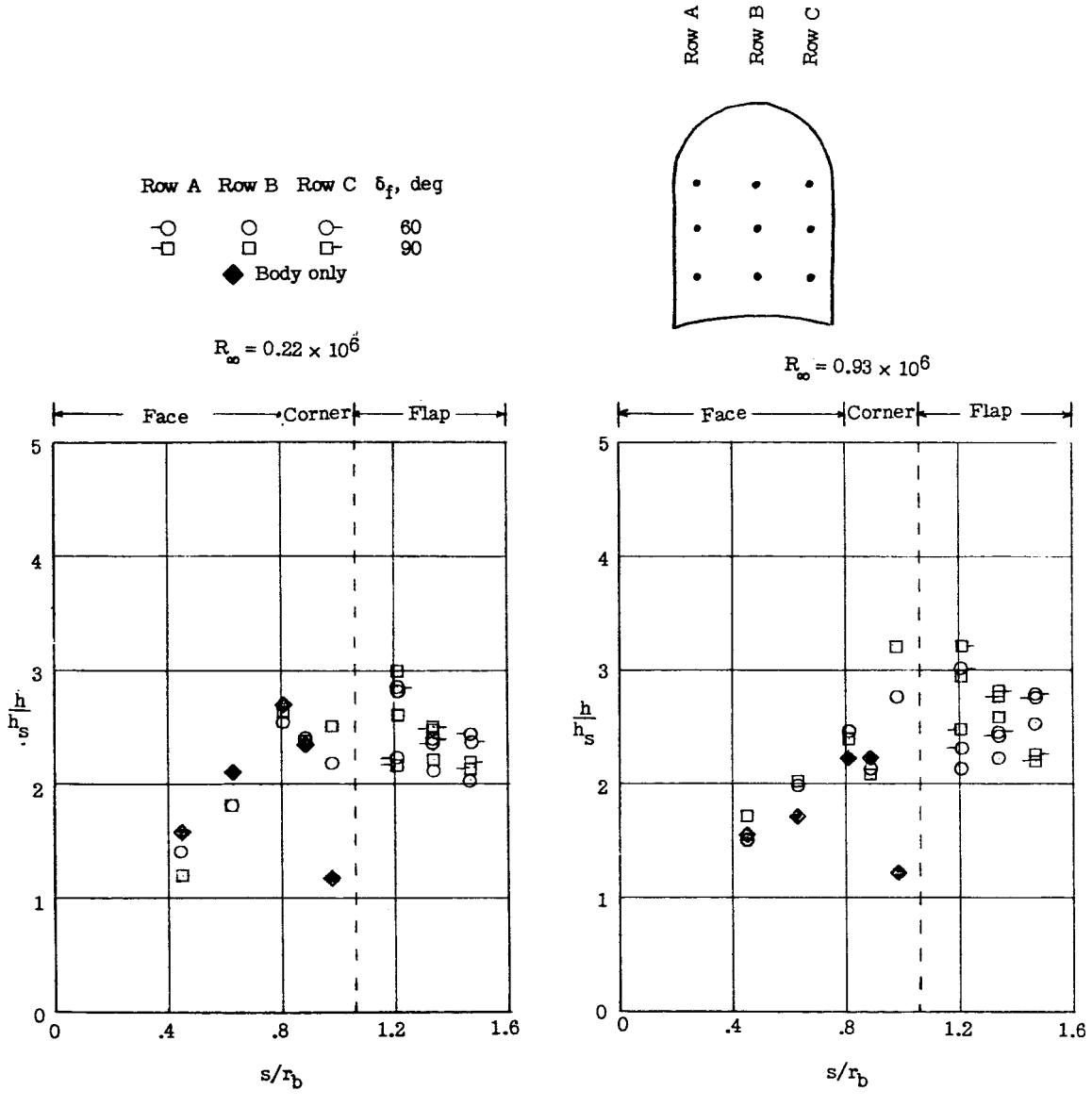

(a) $\alpha = 15^\circ$.

Figure 20.- Heat transfer to windward flap.

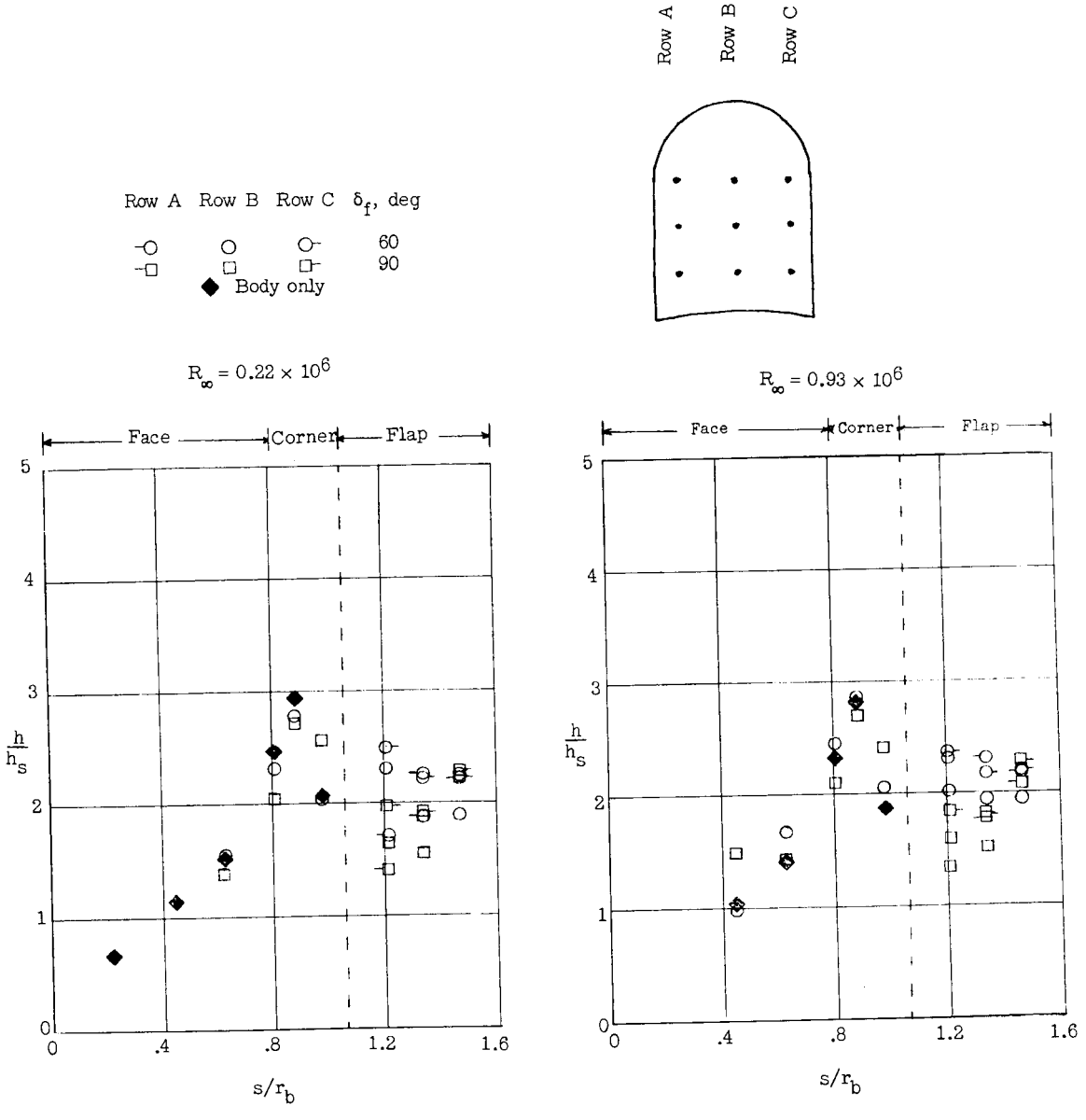

(b) $\alpha = 30^\circ$.

Figure 20.- Continued.

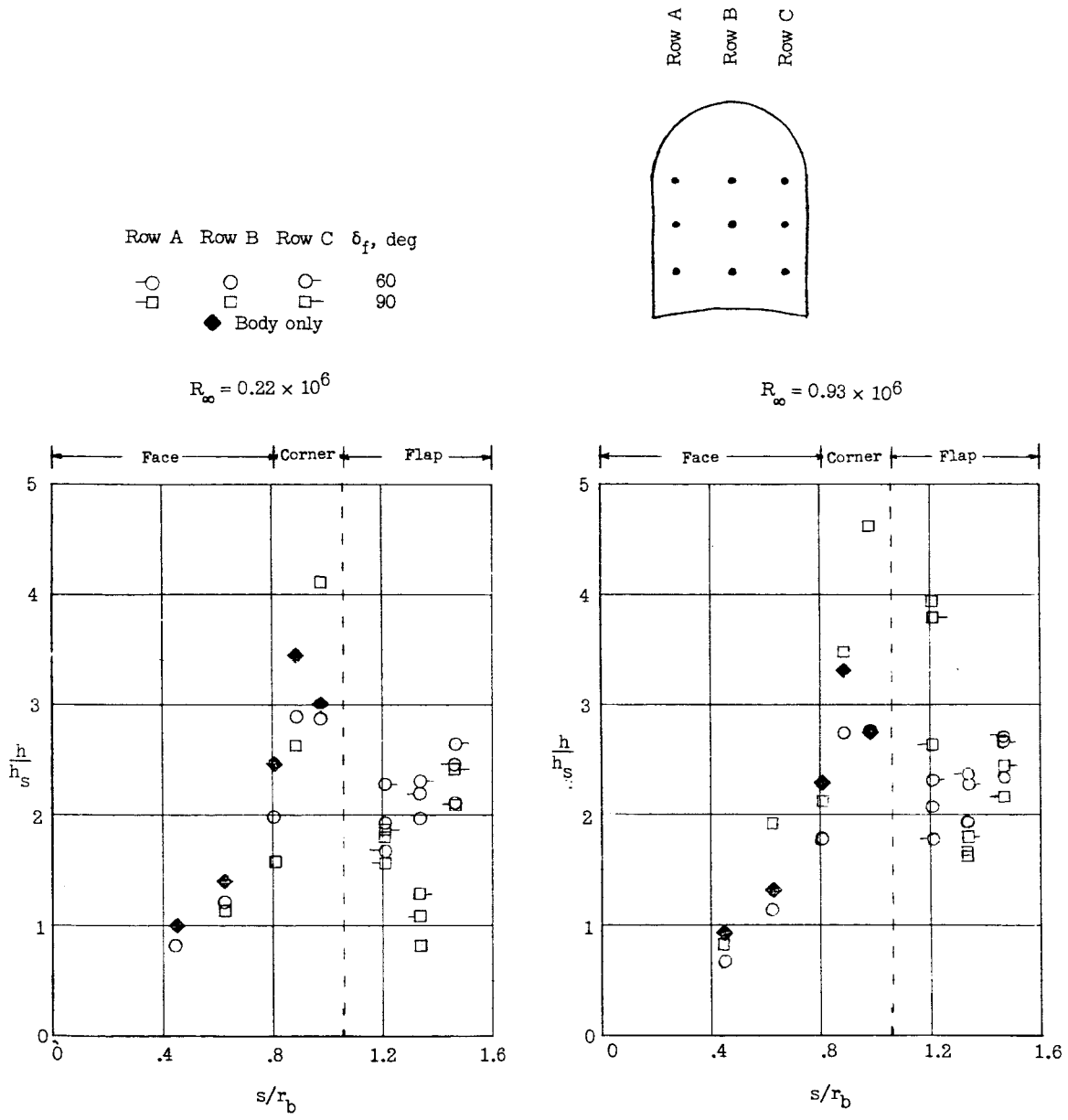

(c) $\alpha = 45°$.

Figure 20.- Concluded.

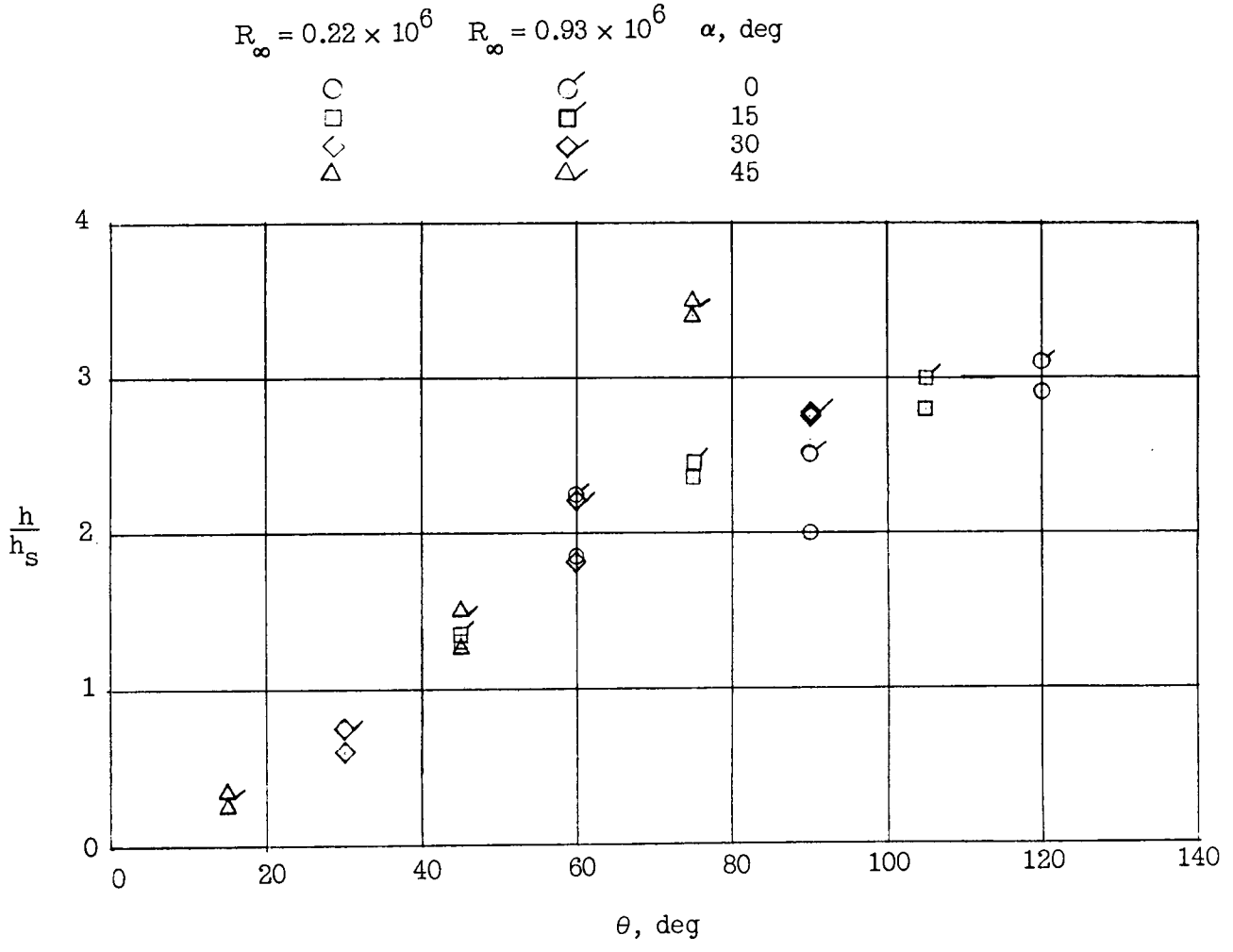

(a) Leeward flap.

Figure 21.- Variation of flap heat transfer with flap angle.

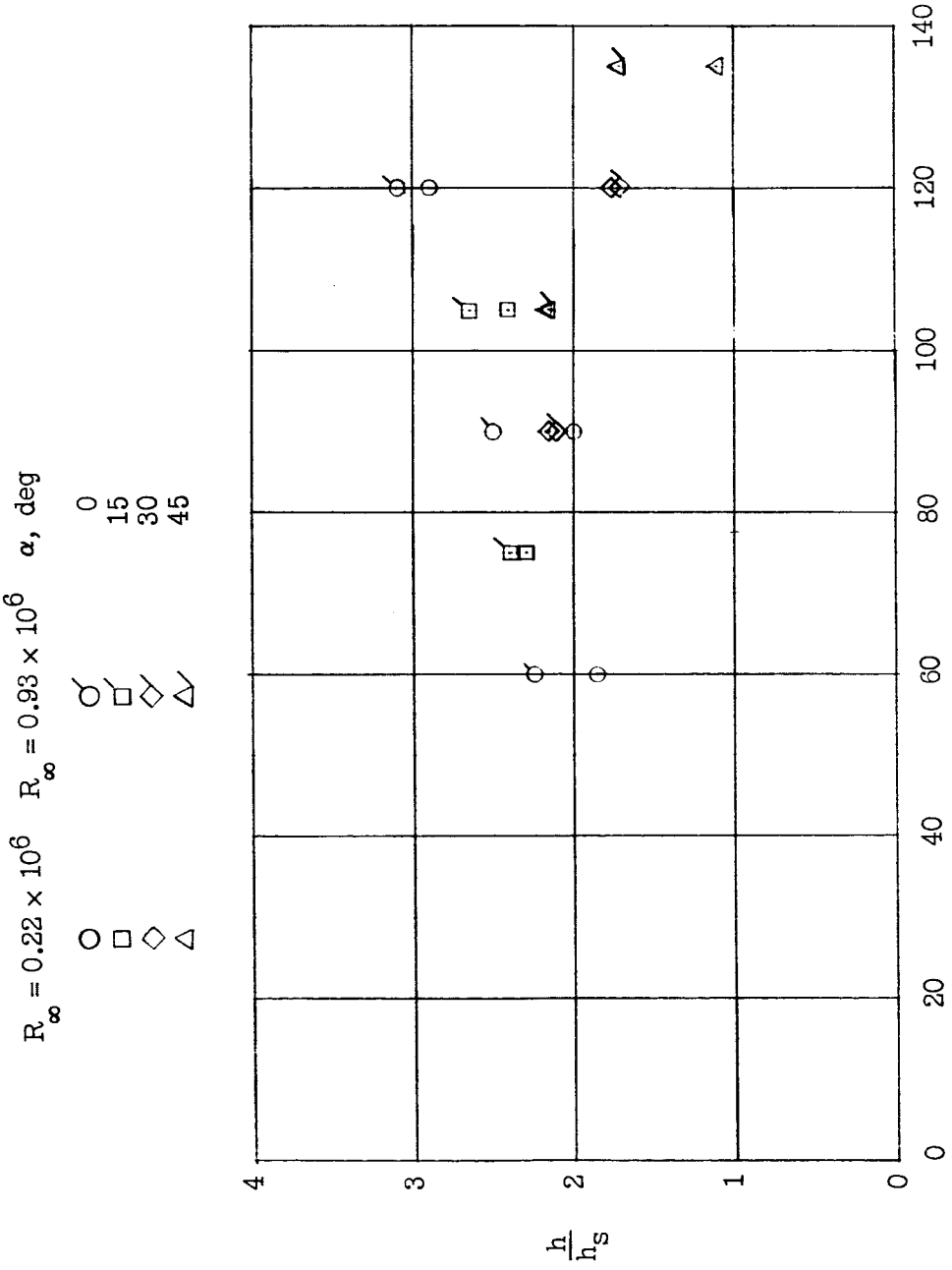

(b) Windward flap.

Figure 21.- Concluded.

NASA-Langley, 1962 L-1885